

# Bulletin of the Seismological Society of America

## Ground-Motion Variability for Single Site and Single Source through Deterministic Stochastic Method Simulations: implications for PSHA

--Manuscript Draft--

<b>Manuscript Number:</b>	BSSA-D-15-00377R3
<b>Article Type:</b>	Article
<b>Section/Category:</b>	Regular Issue
<b>Full Title:</b>	Ground-Motion Variability for Single Site and Single Source through Deterministic Stochastic Method Simulations: implications for PSHA
<b>Corresponding Author:</b>	Maria D'Amico, PhD Istituto Nazionale di Geofisica e Vulcanologia Milano, ITALY
<b>Corresponding Author's Institution:</b>	Istituto Nazionale di Geofisica e Vulcanologia
<b>Corresponding Author E-Mail:</b>	maria.damico@ingv.it
<b>Order of Authors:</b>	Maria D'Amico, PhD Mara Monica Tiberti, PhD Emiliano Russo, Dr Francesca Pacor, Dr Roberto Basili, PhD
<b>Abstract:</b>	<p>The ground motion median and standard deviation of empirical Ground Motion Prediction Equations (GMPEs) are usually poorly constrained in the near-source region due to the general lack of strong motion records. Here we explore the use of a deterministic-stochastic simulation technique, specifically tailored to reproduce directivity effects, to evaluate the expected ground motion and its variability at a near-source site and seek a strategy to overcome the known GMPEs limitations. To this end, we simulated a large number of equally-likely scenario events for three earthquake magnitudes (M7.0, M6.0 and M5.0) and various source-to-site distances. The variability of the explored synthetic ground motion is heteroscedastic, with smaller values for larger earthquakes. The standard deviation is comparable with empirical estimates for smaller events and reduces by 30-40% for stronger earthquakes. We then illustrate how to incorporate directivity effects into PSHA analysis. This goal is pursued by calibrating a set of synthetic GMPEs and reducing their aleatory variability (~50%) by including a predictive directivity term that depends on the apparent-stress parameter obtained through the simulation method. Our results show that, for specific source-to-site configurations, the nonergodic PSHA is very sensitive to the additional epistemic uncertainty that may augment the exceedance probabilities when directivity effects are maximized.</p>
<b>Author Comments:</b>	
<b>Suggested Reviewers:</b>	
<b>Opposed Reviewers:</b>	
<b>Response to Reviewers:</b>	As suggested by the AE we just made some little modification to the English. We also added the authors list in the electronic supplement.

# Ground-Motion Variability for Single Site and Single Source through Deterministic Stochastic Method Simulations: implications for PSHA

Maria D'Amico<sup>1</sup>, Mara Monica Tiberti<sup>2</sup>, Emiliano Russo<sup>2</sup>, Francesca Pacor<sup>1</sup>, Roberto Basili<sup>2</sup>

<sup>1</sup>*Istituto Nazionale di Geofisica e Vulcanologia, Via Corti 12, 20133 Milan, Italy*

<sup>2</sup>*Istituto Nazionale di Geofisica e Vulcanologia, Via di Vigna Murata 605, 00143 Rome, Italy*

## Abstract

The ground motion median and standard deviation of empirical Ground Motion Prediction Equations (GMPEs) are usually poorly constrained in the near-source region due to the general lack of strong motion records. Here we explore the use of a deterministic-stochastic simulation technique, specifically tailored to reproduce directivity effects, to evaluate the expected ground motion and its variability at a near-source site and seek a strategy to overcome the known GMPEs limitations.

To this end, we simulated a large number of equally-likely scenario events for three earthquake magnitudes (M7.0, M6.0 and M5.0) and various source-to-site distances. The variability of the explored synthetic ground motion is heteroscedastic, with smaller values for larger earthquakes. The standard deviation is comparable with empirical estimates for smaller events and reduces by 30-40% for stronger earthquakes.

We then illustrate how to incorporate directivity effects into PSHA analysis. This goal is pursued by calibrating a set of synthetic GMPEs and reducing their aleatory variability ( $\sim 50\%$ ) by including a predictive directivity term that depends on the apparent-stress parameter obtained through the simulation method. Our results show that, for specific source-to-site configurations, the nonergodic PSHA is very sensitive to the additional epistemic uncertainty that may augment the exceedance probabilities when directivity effects are maximized.

30 The proposed approach may represent a suitable way to compute more accurate hazard estimates.

31 **Key words:** *seismogenic sources, finite fault simulations, near source, directivity effects, ground*  
32 *motion variability, seismic hazard, Southern Italy*

33

## 34 **Introduction**

35 Practical seismic hazard applications require the ground motion component to be explored for  
36 various possible events that could affect a site of interest. The hazard assessment can either be  
37 carried out through probabilistic or deterministic approaches with the main difference between the  
38 two methods residing in the time variable, which is absent in the deterministic method (Bommer,  
39 2002). A probabilistic approach typically explores all possible earthquake magnitudes, above a  
40 given minimum, sampled from an established Frequency-Magnitude Distribution (FMD), usually in  
41 the form of a Gutenberg-Richter power law generated by all possible seismic sources. Conversely,  
42 deterministic approaches usually explore one or few controlling events generated by one or few  
43 seismic sources. The controlling event or events could be the Maximum Credible Earthquake (e.g.  
44 Mualchin, 1996), or the earthquakes that may cause a pre-defined level of damage or malfunction  
45 (e.g. for nuclear facilities the Seismic Level 1 or Seismic Level 2; IAEA, 2002, 2010).  
46 Recommendations on how to carry out these analyses are included in regulations for designing new  
47 buildings or critical infrastructures or for retrofitting purposes (e.g. ASCE, 2005, 2010; BSSC,  
48 2009). Other fields of interest, however, are also the preservation of cultural heritage and the  
49 actions undertaken for civil protection purposes (e.g. training and plans for emergency response and  
50 post-earthquake recovery).

51 For both the probabilistic and deterministic approaches, the accuracy of the predicted ground-  
52 motion amplitude is a fundamental issue (McGuire, 1995; Chapman, 1995; Bazzurro and Cornell,  
53 1999; McGuire, 2001), especially when the analyzed site and the seismic source are very close one  
54 to another. In such a case, the ground motion median and standard deviation evaluated from any  
55 Ground Motion Prediction Equation (GMPE) are usually poorly constrained due to the general lack

56 of strong motion records in near-source conditions. In addition, the ground motion variability  
57 associated with a single fault is even more difficult to be assessed because multiple records of  
58 earthquakes generated by the same fault rarely exist. Finite-fault simulations can represent a valid  
59 alternative to overcome the limitations of GMPEs, especially in the near-source region, where the  
60 ground motion is dominated by effects due to the finiteness of the source, such as directivity, fault  
61 hanging-wall/foot-wall relative position to the site, radiation-pattern, and slip distribution.  
62 Directivity effects, in particular, have the largest impact on the ground motion variability at low and  
63 intermediate frequencies, causing amplification at sites in the forward direction of the rupture  
64 (Ruiz-García, 2011).

65 The use of numerical simulations is recently increasing and a number of initiatives worldwide are  
66 promoting their application for hazard assessment purposes (Graves et al., 2010; Dreger and Jordan,  
67 2015). The CyberShake Project promoted by the Southern California Earthquake Center (Graves et  
68 al., 2010), extensively utilizes 3D numerical simulations coupled with kinematic source models to  
69 compute low-frequency ground motions (up to 0.5Hz) and assess deterministic and probabilistic  
70 seismic hazard in Southern California. The related hazard maps differ from the classical ones based  
71 on empirical GMPEs for including long-period effects, such as basin and directivity effects.  
72 Although these methods improve the ground motion description, they require very high-  
73 performance computational resources to be applied on a routinely basis.

74 One possible strategy to inject simulated ground motion into Probabilistic Seismic Hazard Analysis  
75 (PSHA) is by means of the computation of generalized attenuation functions (GAFs). GAFs replace  
76 the empirical predictions with large sets of numerical simulations from which derive the first two  
77 moments of the ground motion parameters probability distributions (Convertito, 2006; Faccioli,  
78 2013; Villani et al., 2014). The GAFs can be generated with different simulation codes (purely  
79 deterministic, stochastic, hybrid) depending on the target of the hazard analysis, but they should be  
80 validated beforehand by the comparison with observed records (Goulet et al., 2015). Convertito  
81 (2006) used a high-frequency deterministic technique for the prediction of the ground motion in a

82 characteristic earthquake and showed the effect of the source radiation pattern and directivity at  
83 several sites around the fault. Villani et al. (2014) used 3D numerical simulations to demonstrate  
84 how near-source high-resolution representation of hazard, which accounts for combined 3D effects  
85 (site effects, basin effects, and topographic features), is more realistic than those purely based on  
86 traditional GMPEs.

87 In this work, we explore the use of a deterministic-stochastic simulation method (DSM, Pacor et al.,  
88 2005) to predict the ground motion close to the source, assess its variability, and calibrate synthetic  
89 attenuation models - including directivity effects - to be incorporated into PSHA. This study is  
90 timely in order to integrate the selection of GMPEs for the current update of the Italian seismic  
91 hazard map (MPS16, see Data and Resources).

92 To this end, we set up a case study for the city of Cosenza, southern Italy, a densely populated city  
93 with a rich heritage of historic buildings, located in one of the Italian regions characterized by the  
94 highest seismic hazard (as for the MPS04, the Italian official seismic hazard map, Figure 1a;  
95 Gruppo di Lavoro MPS, 2004), a long history of damaging earthquakes (Figure 1c), and a site  
96 where only few strong motion data are available (Luzi et al., 2008; Pacor et al., 2011).

97 The expected ground motion is evaluated for bedrock and free-field conditions, at a single target  
98 site located in the proximity of a single fault (SFSS: Single-Fault Single-Site scenarios) assumed as  
99 capable of generating from moderate to strong earthquakes. As a modeling strategy, we generate a  
100 large number of rupture scenarios by varying both the location and kinematic parameters of  
101 individual ruptures. We simulate earthquakes of three magnitude values, M7.0, M6.0, and M5.0, as  
102 well as source-to-site distances of 0 to 10 km (Figure 1b), thereby exploring the range of the major  
103 contribution to PSHA at Cosenza as resulting from the disaggregation analysis of the MPS04  
104 (Figure 1d; Meletti et al., 2007; Martinelli and Meletti, 2008; Stucchi et al., 2011).

105 The median values and variability of ground motion distributions simulated for SFSS conditions are  
106 analyzed to test the performance of the simulation method in reproducing directivity effects in

107 various source-to-site configurations and compared with those predicted by two reference GMPEs  
108 (BSSA, Boore et al., 2014; BI2014, Bindi et al., 2014)  
109 Finally, we discuss some of the possible implications of our results for the PSHA by testing the  
110 influence of directivity effects in the near source region.

## 111 **Sampling the Aleatory Variability of SFSS Scenarios**

112 Although the number of involved elements in the SFSS estimate is minimal (one fault, one site),  
113 each of them involves several parameters which need to be based on prior information affected by  
114 aleatory uncertainty. This represents a typical hazard problem that can be tackled through the Event  
115 Tree (ET) approach (Ericson, 2005) and has already been adopted in a number of geophysical  
116 applications (e.g.: Newhall and Hoblitt 2002; Lorito et al., 2015; Selva et al, 2016). Here, we use a  
117 simplified ET-like representation of our experiment where each ET branch represents possible  
118 realizations of earthquake rupture models exploring various characteristics of earthquake source and  
119 target site. For simplicity, we assume a uniform probability distribution of discrete values for all the  
120 parameters of each branch. The procedure to introduce and manage SFSS variability is exemplified  
121 in Figure 2. Extended descriptions of each ET branch used in the Cosenza case study follow.  
122 Alternative models to the one adopted here represent an epistemic uncertainty that is commonly  
123 tackled through the implementation of logic trees or ensemble modeling (Marzocchi et al., 2015).  
124 However, the thorough treatment of epistemic uncertainty is beyond the scope of this work.

## 125 **ET implementation**

### 126 **Branch #1: Parent Fault and its context**

127 The case study is set in the area source (AS) 929 “Calabria tirrenica” of the seismic zonation ZS9  
128 (Meletti et al., 2008) at the base of MPS04 (Gruppo di Lavoro MPS, 2004), a tectonically active  
129 region of southern Italy dominated by E-W extensional tectonics (e.g. Meletti et al., 2008) and  
130 prevailing N-S maximum horizontal stress (Carafa and Barba, 2013).

131 A single Parent Fault (PF) is defined here by a rectangular fault plane adopted from the DISS 3.1.1  
132 (DISS Working Group, 2010; Basili et al., 2008) and consisting of a north-south striking, west-

dipping, normal fault (Figure 1a and Table 1). The target site (city of Cosenza; CSZ) is located on the hanging wall of this fault.

## **Branch #2: Child Faults Generation**

A Child Fault (CF) is a fault that inherits orientation and sense of movement from the PF defined in Branch #1 and other static parameter according to a selection of possible earthquake magnitudes. We adopt three earthquake moment magnitudes: M5.0, M6.0, and M7.0, that encompass the range of magnitudes ( $M = 5.5-6.0$ ) that dominates the ground motion (Peak Ground Acceleration) at Cosenza for near-site seismic sources at short (475 years) and long (2476 years) average return periods (ARP) (Figure 1d). For each magnitude value we obtain the equivalent seismic moment using the classical relationships by Kanamori and Anderson (1975) and Hanks and Kanamori (1979) and deriving fault area and slip from seismic moment, assuming a rigidity of 30 GPa. Length and width (rounded values) are then determined by assuming an aspect ratio of  $\sim 1.5$  (Table 2).

## **Branch #3: Scenario Set**

This branch explores the range of possible source-to-site configurations. In our case, the CFs are irregularly distributed over the PF (Figure 1b) with a smaller spacing for the shallower sector to better explore the closest distances from the site. For M7.0 we consider only one CF, with the top edge at 1 km depth, covering almost the entire PF plane. For M6.0 we consider five identical CFs, distributed at a regular spacing of half fault length, from north to south, along the uppermost part of the M7.0 CF. For M5.0 there are 23 identical CFs distributed at five irregular depth levels (Table 2).

## **Branch #4: Scenario Events**

Since the specific kinematic features of any future rupture on the CFs defined at Branch #2 and #3 are unknown, we generate a large number of possible scenario events for each magnitude (Table 3). The aleatory variability of the rupture process is incorporated by varying rupture kinematics within plausible a-priori defined parameter ranges (Table 1). Several scenario events are obtained by varying the position of the nucleation points and considering rupture fronts that radially propagate with three different constant velocities  $V_r$  (Table 1). The M7.0 CF is subdivided along strike into

three sub-faults for each of which we simulate nine nucleation points at a regular spacing of 3 km along strike and 4.5 km along dip (Table 3). In such a way, both unilateral and bilateral directivity effects can be properly modeled. Being the M6.0 CFs smaller, we simulate only nine nucleation points uniformly distributed on the fault plane at a regular spacing of 4 km along strike and 3 km along dip (Table 3). For the M5.0 CFs we simulate only three nucleation points with a regular spacing of 1 km in the middle of the fault plane (Table 3).

Fault slip is assumed as uniformly distributed over each CF plane. Although this hypothesis may seem very simplistic, we use it because in the simulation method adopted in this study the slip distribution has a second-order effect on the ground motion amplitude (Pacor et al., 2005) if compared to the other kinematic parameters (i.e. nucleation point and rupture velocity).

#### **Branch #5: Propagation Medium Properties**

We use a 1D multilayer model (Table 4) considered representative of the study area in agreement with seismic imaging studies for southern Italy (Barberi et al., 2004; Orecchio et al., 2011; D'Amico et al., 2011). The anelastic attenuation (Table 1) is obtained through a constant quality factor from Rovelli et al. (1988). For simplicity we use only the expected values of each layer. Given the very short source-to-site distance ( $R_{JB} < 15$  km), we use an inverse-distance geometrical spreading factor ( $1/R$ ) to model the path effects (Table 1).

#### **Branch #6: Site Conditions**

All simulations are performed at bedrock and free-field conditions assuming three values for the attenuation at high frequency, described by the  $k_0$  parameter (Table 1) and selected among typical values for rock sites (Anderson and Hough, 1984; Boore and Joyner, 1997; Parolai and Bindi, 2004).

#### **Branch #7: Receivers Geometry**

The distribution of virtual receivers deployed in the region of interest includes two sites (Figure 1): CSZ is located in the middle of the M7.0 CF, and s001 is located close the northernmost edge of the fault. Simulations for the M7.0 are performed for both CSZ and s001 to analyze the ground-motion



185 variability due to bilateral and quasi-unilateral directivity effects, respectively.  $R_{JB}$  is equal to zero  
186 for both sites. For the M6.0 CFs  $R_{JB}$  varies between 0-7 km. For the M5.0 CFs  $R_{JB}$  is equivalent to  
187 the epicentral distance and varies between 0-15 km (Table 2).

## 188 **SFSS scenario output and analysis**

189 A remarkable number of acceleration time series is generated for each earthquake magnitude (Table  
190 3) to ensure the statistical significance of SFSS simulated ground motions. The expected seismic  
191 shaking can thus be represented by the distributions of Intensity Measure Types (IMTs) commonly  
192 used for engineering purposes rather than using values inferred from single scenario events.  
193 However, the ET scheme produces several scenarios and it is thus necessary to sample a restricted  
194 dataset of synthetic waveforms able to reflect the overall ground-motion variability, which meet the  
195 various engineering requirements. In general, once the simulation results are obtained, a  
196 comparative scheme has to be adopted to ensure the reliability of synthetic IMTs (e.g. comparing  
197 synthetic distributions with pre-existing empirical models or, when available, with recorded data).

## 198 **Simulation Method**

199 The Deterministic Stochastic Method (DSM, Pacor et al., 2005) is an extension of the stochastic  
200 point source simulation method of Boore (1983, 2003) and it is designed to reproduce the  
201 directivity effects due to the rupture propagation along an extended fault. Despite the simplistic  
202 modeling of the physics of rupture generation and propagation, DSM was successfully used for  
203 estimating ground motion variability located near active faults (Carvalho et al., 2008; Ameri et al.,  
204 2008). In several studies, DSM was able to reproduce the main features of the observed short-period  
205 ground motions (Cultrera et al., 2010), with results comparable to those computed by hybrid  
206 techniques (Ameri et al., 2009, Ameri et al., 2011).

207 In the DSM, the source model is described by a rupture radially propagating with constant velocity  
208 from a nucleation point along a finite fault, and by a slip distribution. DSM exploits the isochrones  
209 theory (Bernard and Madariaga, 1984; Spudich and Frazer, 1984) to compute the envelopes of the

210 acceleration signals, to define the apparent corner frequency, and to estimate the source-to-site  
211 distance.

212 For each site the envelope is built by summing the contributions to ground motion from the  
213 corresponding isochrone on the fault. A random phase modulates the amplitude of the medium  
214 response to ensure that the envelopes are calculated as incoherent summation of the energy emitted  
215 by each point of the fault. The duration and shape of the envelope are functions of the rupture  
216 model (fault dimensions, rupture nucleation point, and rupture velocity) and of the relative fault-to-  
217 receiver position. The envelope varies from site to site and describes how the site perceives the  
218 energy released from the source.

219 For a given site, the spectral content of the synthetic seismogram is then defined through the finite-  
220 fault reference spectrum  $FFR(f)$ , given by:

$$221 \quad FFR(f) = S(f) \cdot A(f) \cdot K(f) \quad (1)$$

222 where  $S(f)$  is the apparent source acceleration spectrum,  $A(f)$  is the attenuation operator, and  $K(f)$  is  
223 the site response function.

224  $A(f)$  includes the geometrical spreading and the frequency-dependent attenuation term in the form:

225  $A(f) = G(R) \exp \left[ \frac{-\pi f R}{Q(f) \beta} \right]$ , where  $G(R)$  is the geometrical spreading attenuation,  $\beta$  is the shear-wave  
226 velocity,  $Q$  is the apparent quality factor (values reported in Table 1). As the simulations are  
227 performed at bedrock, the only site effect considered is the high-frequency attenuation introduced  
228 through the Anderson and Hough's (1984) model given by  $K(f) = \exp(-k_0 \pi f)$ , where  $k_0$  is the  
229 parameter describing the spectral decay.

230 The radiation pattern  $R_{\theta\phi}$ , the source-to-site distance  $R$ , and the corner frequency are inferred by  
231 deterministic envelopes in order to take into account the effects of the rupture propagation along a  
232 finite fault (Pacor et al., 2005). The source-to-site distance and the radiation pattern adopted to scale  
233 the reference spectrum at each receiver are determined through a spatial average over the entire  
234 fault, followed by a temporal average, weighted by the envelope function itself (global average).

235 The spatial average can also be performed over the reduced fault area associated with the maximum  
 236 pulse of energy arriving at a given site, defined by the maximum isochrone velocity (local average).  
 237 The apparent source acceleration spectrum  $S(f)$  has the shape of the classical omega-square model  
 238 (Brune 1970):

$$239 \quad S(f) = C \cdot M_0 (2\pi f)^2 \frac{1}{1 + \left(\frac{f}{f_a}\right)^2} \quad (2)$$

240 where  $C$  is a constant given by  $\frac{\Re_{\theta\varphi} F}{4\pi\rho\beta^3}$ , (where  $\Re_{\theta\varphi}$  is the radiation pattern;  $F$  is the free-surface  
 241 amplification, and  $\rho$  is the density),  $M_0$  denotes the seismic moment, and  $f_a$  is the apparent corner  
 242 frequency. Differently from the point-source model, the corner frequency is defined as the inverse  
 243 of the envelope duration and it differs from site to site (apparent corner frequency). By means of the  
 244 apparent corner frequency, the directivity effects are directly included in the simulation,  
 245 reproducing the expected azimuthal variation of corner frequency and spectral amplitudes due to the  
 246 source rupture propagation. Consequently, the ground motion simulated at sites along the direction  
 247 of the rupture front propagation experience (forward/backward) directivity-induced  
 248 amplification/attenuation effects. Note that, due to the relationship between stress drop and corner  
 249 frequency (Brune, 1970), from the apparent corner frequency it is possible to evaluate an apparent  
 250 stress parameter that can be used to measure to what extent the site is affected by directivity effects.  
 251 Similarly, the earthquake stress parameter can be obtained from the corner frequency of the event,  
 252 given by the inverse of the rupture duration.

253 In the context of the stochastic finite-fault modeling, the largest source of epistemic uncertainty in  
 254 the ground motion prediction is due to the limited knowledge concerning the stress drop  
 255 (Motazedian and Atkinson, 2005; Atkinson and Boore, 2006), which is the main “free” input  
 256 parameter that controls the level of the acceleration spectrum ( $> 1$  Hz). In DSM, this issue is  
 257 addressed by replacing the epistemic uncertainty on the stress parameter with the aleatory  
 258 uncertainty given by the variability in the fault dimension, nucleation point, and rupture velocity.

Figure 3 shows the range of variability of the apparent stress parameter  $\Delta_{app}$  and local distance associated to the ET implementation presented in the previous section. The “apparent” stress parameters vary in different ranges for different magnitudes, with the widest range for the M5.0 class in which several faults, with different rupture velocities and distance-to-source geometries are involved. Conversely, the local distances are very similar to the hypocentral distance for M5.0 while they shorten as the fault dimension increases.

In this work, to test the influence of the use of the apparent corner frequency (or apparent stress parameter) in the evaluation of ground motion amplitudes at a single site, we considered three different setups of the DSM (M1, M2, and M3). Each setup has the role to differently weight directivity effects as follows:

- i) M1 (maximum directivity effect): prescribes the use of the deterministic envelope duration to define the apparent corner frequency  $f_a$ ; in this way, the corner frequency depends on rupture velocity, nucleation point, fault dimension, and relative position of the observer with respect to the nucleation point.
- ii) M2 (minimum directivity effect): uses the fixed corner frequency, defined by an apparent stress parameter of 30 bar; in this case, the finite-source effects are taken into account only in the distance and radiation pattern computation.
- iii) M3 (medium directivity effect): implies the use of a minimum threshold  $f_{th}$  for the apparent corner frequency in order to minimize backward directivity effects simulated by M1 and not clearly observed on recorded data; for each magnitude class  $f_{th}$  is defined by a constant value for the apparent stress parameter of 30 bar (i.e. for  $M = 7$   $f_{th} = 0.07$  Hz,  $M3 = M2$  if  $f_a \leq f_{th}$ , otherwise  $M3 = M1$ ).

In the three cases, we use the local metrics definition both for  $R_{\theta\phi}$  and  $R$ . Compared to the global metrics, the local one produces larger ground-motion variability and, on average, higher amplitudes.

## Analysis of the Synthetic Ground Motion Dataset

### Median and standard deviation of the simulated ground motion

285 Figure 4 shows the box plots of the peak ground acceleration (PGA) and peak ground velocity  
 286 (PGV) synthetic distributions (geometrical mean of the horizontal components), obtained by the  
 287 M1, M2, and M3 DSM setups for the three magnitudes classes ( $\log_{10}$  units). For M7.0, the ground  
 288 motion distributions are relative to the bilateral CSZ and the quasi-unilateral s001 sites (Figure 1),  
 289 both located at a Joyner-Boore distance  $R_{JB} = 0$ . In the cases of M6.0 and M5.0, the involved  $R_{JB}$   
 290 varies in the range 0-7 km and 0-15 km, respectively (Figure 1). We aggregate the synthetic  
 291 ground-motion peak values at 0 or 5 km for M6.0. For M5.0,  $R_{JB}$  varies with depth because the PF  
 292 is inclined. We thus aggregate the  $R_{JB}$  distances into two depth groups that contain approximately  
 293 the same number of realizations. The resulting mean  $R_{JB}$  distances are of 5 km and of 10 km,  
 294 respectively. We introduced this approximation to explore the synthetic ground motion variability  
 295 for two different source-to-site distances and to compare our results with median and variability  
 296 ground motion predicted by GMPEs. The median ( $\mu_{DSM}$ ) and standard deviation ( $\sigma_{DSM}$ ) of the DSM  
 297 distributions are reported in Table 5 and Table 6, respectively. Ground motion distributions are  
 298 shown in the Electronic Supplement. For M7.0 and M6.0, based on visual inspection and statistical  
 299 tests (i.e. Kolmogorov-Test,  $\chi$ -square test with 5% confidence interval), the synthetic PGAs follow,  
 300 on average, a lognormal distribution, independently of the modeling setups (M1, M2, and M3).  
 301 However, directivity effects can generate distributions characterized by a positive or negative skews  
 302 (for example the PGA distributions at s001 relative to M7.0). Compared to the PGAs, the PGV  
 303 values are better described by multimodal distributions. For M5.0 we observe that, independently  
 304 from the scenario model, the ground-motion parameter distributions can be only approximated by  
 305 lognormal shapes both at high and low frequencies; a larger number of CFs should be considered to  
 306 better sample the PF to generate a lognormal distribution.

307 The weight assigned to the directivity effects for the three modeling setups influences the ground  
 308 motion distributions: in general, the median values are lower for M1 and higher for M3, whereas  
 309 the associated variability shows opposite trends. These features are especially marked in the case of  
 310 the quasi-unilateral site (s001) for M7.0, and for the more distant faults of M6.0 and M5.0 in which

311 forward and backward directivity effects dominate, due to the particular source-to-site  
 312 configurations. For all the three magnitudes, the variability in M1 is about 40% and 30% larger than  
 313 in the M2 and M3 configurations, respectively. When the contribution of the apparent corner  
 314 frequency is limited, either by a fixed corner frequency (M2) or by a threshold in the apparent  
 315 corner frequency (M3), the ground-motion variability is mainly controlled by the variability of local  
 316 distance and radiation pattern. In these cases, the contribution of the backward directivity is  
 317 minimized or partially reduced, thus increasing the median values and reducing the range of  
 318 simulated values. As the magnitude decreases, the synthetic ground motion variability increases: the  
 319 standard deviations vary from 0.18 for M7.0 to 0.38 for M5.0 (Table 6).

320 In our modeling, the synthetic variability represents the ground motion variability expected at a  
 321 single site over many scenario events on a given fault and includes: i) the source term, given by  
 322 various kinematic scenarios; ii) the site term, related to the three considered bedrock conditions; iii)  
 323 the synthetic-to-synthetic term, due to the simulation of forward and backward directivity effects at  
 324 the same site. For the smallest events, a further source of variability is related to the uncertainties of  
 325 the CFs locations over the PF, thus generating a large dispersion in the simulated ground motion.  
 326 This finding is in agreement with recent empirical heteroscedastic GMPEs that found a decrease of  
 327 the scatter with increasing magnitude (e.g., Bommer et al., 2007; Boore et al., 2014). Among the  
 328 possible causes, errors in the location and magnitude determination of smaller events, in particular  
 329 aftershocks, might contribute to the larger scatter for smaller events (Strasser et al., 2008).

330 Figure 5 shows the synthetic cumulative distribution functions (CDFs) of PGA, computed at CSZ  
 331 considering the three magnitude classes and the M1 setup; this will help to better understand how  
 332 uncertainties of different input simulation parameters contribute to the ground-motion variability.  
 333 For M6.0 and M5.0, the analyses are carried out considering the largest distance bin. In Figure 5a,  
 334 the three CDFs are related to each rupture velocity: we grouped the scenarios with a fixed  $V_r$  and  
 335 variable nucleation point position and  $k_0$ . In Figure 5b, the CDFs are calculated for the three  $k_0$

336 values. In Figure 5c the scenarios are grouped considering three nucleation areas, each of them  
337 corresponding to one third of the parent fault.

338 The variation of rupture velocity and  $k_0$  contributes to the ground motion variability. The CDFs in  
339 Figure 5a are shifted to larger PGA values as the selected  $V_r$  increases. A similar trend is observed  
340 for  $k_0$  values but in a small extent. The effect of the nucleation area (Figure 5c) is more complicated  
341 because it depends on the position of CSZ compared to the CFs. On the one hand, the M7.0  
342 nucleation areas 1 and 3 produce very similar PGA distributions, which are lower than the one of  
343 area 2. On the other hand, for M6.0 the opposite occurs and areas 1 and 3 generate the largest  
344 ground motions. In general, uncertainties in the hypocenter position produce a large variability of  
345 ground motion as can be observed for M5.0, where the CDFs are also distinguished in relation to  
346 the depth of the hypocenters.

## 347 **Comparison with GMPEs**

348 In this section we compare the synthetic ground motion medians and variances with the predictions  
349 from global (BSSA, Boore et al., 2014) and Pan-European (BI2014, Bindi et al., 2014) GMPEs, for  
350 the rock-soil category and for various magnitude-distance (M-R) pairs (Table 2, and Figure 6a).

351 Here we have two objectives: one is to test the reliability of our simulations, while ensuring that the  
352 combinations of input parameters produce ground-motion levels that are consistent with the  
353 observations for similar conditions; the other is to assess to what extent the ground-motion  
354 variability and median values of empirical models may represent directivity effects. Independently  
355 from the DSM setups (M1-3), the synthetic ground motion median values fall within the empirical  
356 median plus/minus one standard deviation, thus supporting the reliability of our modeling (Figure  
357 6a). The standard deviations of the synthetic ground motions are consistent with the empirical ones  
358 for the M6.0 and M5.0 and the M1 configuration, for which more than one fault is involved and the  
359 directivity effects are strongest. In all the other cases the synthetic variability is lower.

360 In the SFSS case and M7.0, the synthetic variability is expected to be lower than the empirical one  
361 obtained from global models that include contributions from multiple sites, paths, and sources

362 (ergodic assumption). For example, Yagoda-Biran et al. (2015) showed that the variance in ground  
363 motions related to repeated large earthquakes (single fault) is reduced by about 45% and 80% with  
364 respect to the between-event variability  $\tau$  of the global model.

365 Figure 6b shows the Probability Density Function (PDF) of PGA as predicted by the BI2014 and  
366 BSSA at CSZ and s001 together with PDFs obtained from M1, M2, and M3 setups for M7.0,  
367 considering a lognormal distribution. Since only a single fault is involved, the total sigma of the  
368 empirical PDFs is computed using the fault-variance defined in Yagoda-Biran et al. (2015) as  $\tau^2/2$   
369 instead of the between-event variance. For comparison, we also consider the sigma estimated for a  
370 single seismic source zone in Italy by Luzi et al. (2014) which is about 30% lower than the overall  
371 sigma for the entire Italian territory. The PGA distribution generated for maximum directivity  
372 effects (M1 setup) is very close to the empirical distributions in terms of median values and  
373 variability both at CSZ and s001, when the sigma of a single source is considered.

374 The weight given to the directivity effects strongly influences the median and the associated  
375 standard deviations of the simulated ground motions, demonstrating how near-source effects are not  
376 adequately represented by traditional GMPEs. Forward directivity effects, in particular, could be an  
377 enhancement of the ground motions of about 60-100% (M3 setup for quasi-unilateral site).

## 378 **Synthetic ground motion models**

379 DSM simulations are used to derive a SFSS ground motion attenuation model accounting for  
380 directivity effects by means of the apparent stress parameter. In this way we carried out our  
381 analyses to account for source-specific and path-specific effects. We adopted this approach with the  
382 dual aim of investigating the contribution of the kinematic ruptures into the overall simulation  
383 variability and evaluating the impact into a simple PSHA performed for the SFSS case study.

384 Villani and Abrahamson (2015) followed a similar approach by identifying repeatable site and path  
385 effects into simulated ground motion variability and assessing the influence of different  
386 assumptions (ergodic, partially ergodic, and fully nonergodic) for the seismic hazard computation.



387 The SSFS model is calibrated for PGA using the hypocentral distance metrics evaluated from the  
 388 nucleation points considered in the ET scheme. In this model, the empirical model BI2014  
 389 describes the attenuation at distances larger than those covered by simulations.

390 As a first step, for each magnitude class and DSM setup, we fit the simulated PGAs using a simple  
 391 distance-dependent function in the form:

$$393 \quad \log(PGA) = c_1 + c_2 \log \frac{R}{d} + \varepsilon \quad (3)$$

$$394 \quad R = \sqrt{R_{hypo}^2 + h_{eff}^2} \quad (4)$$

395 where  $R_{hypo}$  is the hypocentral distance and  $h_{eff}$  is the effective depth parameter that includes near-  
 396 source saturation effects (Atkinson, 2015);  $d$  is the joint distance between synthetic and empirical  
 397 median values and  $\varepsilon$  represents the residuals of the fit,  $c_2$  is a free parameter,  $c_1$  is constrained to  
 398 assume the median value of BI2014 at the joint distance  $d$ . We adopt the Atkinson's (2015)  
 399 relationships, such as  $h_{eff} = \max(1, 10^{(-1.72+0.43M)})$ , for the M7.0 case; in the other two cases we  
 400 adopt the same values ( $h_{eff} = 7.32$ ) suggested by Bindi et al. (2014).

401 Regression coefficients  $c_1$ , and  $c_2$ , and  $h_{eff}$  and  $d$  values are reported in Table 7a, together with the  
 402 standard deviations  $\sigma_{reg}$  for all magnitude classes and simulation setups.

403 Figure 7 shows the comparison between BI2014 and synthetic PGAs ground motion in terms of  
 404 median values and standard deviations. The synthetic median values are generally higher than the  
 405 empirical ones, especially when backward directivity effects are removed (M3). The only  
 406 exception is for the M1 setup with M6.0, where the backward directivity effects dominate because  
 407 of the particular source-to-site configurations. Conversely, the overall synthetic variability is not  
 408 changed with respect to what previously observed. The dispersion remains heteroscedastic with the  
 409 largest values (ever higher than the empirical one) for the M1 setup.

410 To reduce the standard deviation, we introduce the apparent stress parameter ( $\Delta_{app}$ ) as an  
 411 explanatory variable in the previous model. The M1 residuals clearly depend from this parameter,

as illustrated in Figure 8a, indicating that the simple functional form of Eq. 3 is not able to capture the strong directivity effects due to particular combinations of kinematic and geometrical factors. From this example, two remarkable biases with opposite sign are detectable: negative below the 16<sup>th</sup> percentile (~15 bars) and positive above the 84<sup>th</sup> percentile (~30 bars) of the  $\Delta_{app}$  distribution. Negative residuals result from scenario events with ruptures starting in the uppermost part of the fault and propagating with the lowest rupture velocity ( $V_r = 2.4$  km/s); positive residuals are mainly due to up-dip ruptures with the highest rupture velocity ( $V_r = 2.7$  km/s). The residual trend around the median value (~20 bars) of the  $\Delta_{app}$  distribution is unbiased, showing how this cluster is essentially governed by source-to-site distances and the directivity effects are minimized.

As a second step of our regression analysis, we fit the residuals of Eq. 3 through the directivity term depending on  $\Delta_{app}$  according to the following model:

$$\varepsilon = c_3 + c_4 \log(\Delta_{app}) + \varepsilon^* \quad (5)$$

where  $c_3$  is the mean offset of the data with respect to the synthetic attenuation model and  $c_4 \log(\Delta_{app})$  is the contribution of the apparent stress parameter. In Figure 8b we show that the residual trend is almost unbiased and the dispersion is strongly reduced. Regression coefficients  $c_3$  and  $c_4$  are reported in Table 8, together with the standard deviation  $\sigma^*$  for each sampled magnitude and the M1 setup. The most significant result in the strong reduction of the standard deviation of the model of Eq. 3 is the sigma reduction for M7.0. The variability is about 1/3 of the empirical one; it retains the heteroscedastic feature although to a lesser extent. Sigma for M7.0 is about 50% ( $\sigma^* = 0.47\sigma_{reg}$ ) of the variability only considering the hypocentral distance, whereas a major reduction is obtained for lower magnitudes ( $\sigma^* = 0.65\sigma_{reg}$  for M6.0 and  $\sigma^* = 0.72\sigma_{reg}$  for M5.0).

Synthetic ground motion models corrected for the directivity term in the M1 setup are shown in Figure 9 and compared to BI2014 for three percentiles (16<sup>th</sup>, 50<sup>th</sup>, and 84<sup>th</sup>) of the  $\Delta_{app}$  distributions: the median values vary by 30% for M7.0 or by 40% for the lower magnitudes, with respect to the predictions at the 50<sup>th</sup> percentile.

## PSHA sensitivity analysis

438 We employ the set of synthetic attenuation models derived in the previous section to perform a  
439 simplified PSHA sensitivity analyses at CSZ accounting for the area source AS929 of the ZS9  
440 model (Meletti et al., 2008; Figure 10a), whose seismic activity is described by a doubly-truncated  
441 Gutenberg-Richter distribution (with a-value, b-value, and Mmax as shown in Figure 10b), focal  
442 depth, and dominant faulting mechanism as used in MPS04 (Gruppo di Lavoro MPS, 2004). The  
443 integration domain of the hazard integral for CSZ was limited at 30 km distance to isolate only the  
444 single-fault contribution. All the PSHA computations were carried out with the program  
445 CRISIS2015 (Ordaz et al., 2013).

446 In order to exemplify the impact onto the hazard assessment of the synthetic GMPEs accounting for  
447 directivity effects, the annual probabilities of exceedance (APEs) for PGA are computed comparing  
448 the performance of the attenuation models developed in this study with the reference GMPE  
449 BI2014 (Figure 11a). We use for the hazard calculations the sigma values obtained by synthetic  
450 residuals regressions ( $\sigma_{\text{reg}}$  and  $\sigma^*$ ). Such assumption leads toward a total removal of the ergodic  
451 assumption for prevailing path-specific effects, such as those modeled in our stochastic-based  
452 simulations.

453 First, we adopt the model depending on hypocentral distance (Eq. 3). As a result of the comparison  
454 of hazard curves when the ergodic assumption is removed (grey lines), we observe an increased  
455 APE for PGA (Figure 11a). This is due to the overall enhancement of the median ground motion  
456 produced by the synthetic models. The highest hazard curve is for the modeling setup that  
457 minimizes backward directivity. APEs accounting for maximum directivity effects are lower than  
458 the previous case beyond  $1 \text{ m/s}^2$ . When a point-like source is used to represent the ground motion,  
459 the APEs are lower with respect to the other nonergodic hazard curves.

460 Then, we apply the synthetic attenuation model depending on both distance and apparent stress  
461 parameter (Eq. 5). In Figure 11b we show an example of the APEs for this case (nonergodic  
462 assumption). For each magnitude class we select three values of apparent stress parameters  
463 corresponding to the 16<sup>th</sup>, 50<sup>th</sup> and 84<sup>th</sup> percentiles of the distributions plotted in Figure 9. Then, we

464 apply a simplified PSHA logic tree to handle the epistemic uncertainties on the values of the  
465 apparent stress parameters. We build three branches where each of them represents a different  
466 combination of weights. In case of equally-weighted curves each attenuation model has the same  
467 likelihood, whereas in the other two cases, a higher weight is attributed to the synthetic model  
468 defined either by the 16<sup>th</sup> or the 84<sup>th</sup> percentile. We observe how the global effect of the sigma  
469 reduction leads to a decrease of APEs with respect to the ergodic assumption (BI2014). The only  
470 exception is due to the increase in the epistemic uncertainty of the median when forward directivity  
471 effects are accounted for.

## 472 **Discussion and Conclusions**

473 A reliable characterization of the aleatory variability of the ground motion is an important factor in  
474 PSHA because it controls the shape of the hazard curves at low frequencies of exceedance  
475 (Restrepo-Vélez and Bommer, 2003; Bommer and Abrahamson, 2006).

476 The common practice in PSHA is to adopt the total standard deviation of ground-motion models.  
477 However, such models are developed using a broad range of earthquake types, stations, and tectonic  
478 regions. Therefore, the temporal variability of the ground motion for a single source-to-site  
479 combination for a given ARP is assumed to be the same as the spatial variability in ground motion  
480 observed in rich earthquake datasets (i.e. the ergodic assumption; Anderson and Brune, 1999). This  
481 assumption is particularly inappropriate when path-specific effects dominate the ground motion. In  
482 such a case, systematic source-specific and site-specific effects should be removed from the seismic  
483 hazard estimates (Al Atik et al., 2010). This problem can only be tackled by collecting repeated  
484 observations of earthquakes located in a small region nearby the target site. In addition, the GMPE  
485 uncertainty distribution generally follows a lognormal distribution and the misfit between observed  
486 and predicted ground motions is commonly assumed to be homoscedastic, i.e. independent from the  
487 explanatory variable, such as magnitude or distance. However, in several cases the observed  
488 decreasing scatter with increasing magnitude suggests that heteroscedastic models should be used  
489 (Ambraseys et al., 2005; Akkar and Bommer, 2007a,b; Bommer et al., 2007 among others).

490 In this work, we evaluated the ground motion variability related to a SFSS configuration through  
 491 deterministic-stochastic earthquake simulations to investigate the impact of synthetic attenuation  
 492 models in seismic hazard assessment. According to hazard disaggregation from the Italian seismic  
 493 hazard map (MPS04: Meletti et al., 2007; Martinelli and Meletti, 2008) for the site of interest (CSZ;  
 494 Figure 1), our simulations span the entire range of the most contributing earthquake magnitudes in  
 495 near-source conditions (source-to-site distance shorter than 10 km) for short (M5.5 for 475 years)  
 496 and long (M6.5 for 2476 years) ARPs.

497 We modeled only M5.0, M6.0, and M7.0 earthquakes generated by various ruptures laying on the  
 498 same fault plane. Other earthquakes, especially the smaller ones, can likely be generated by other  
 499 faults not considered in this work, such as conjugated and secondary faults, splay faults, and tear  
 500 faults. Other major faults could also exist in the region. These potential seismic sources can further  
 501 increase the variability of the expected ground motion at the site with respect to what we have  
 502 analyzed here. A complete site-specific hazard assessment should also take these potential sources  
 503 into account. An additional source of variability may also come from the slip distribution,  
 504 especially for the larger earthquakes, but this aspect was not modeled in our study.

505 We found that, although synthetic ground-motion median values are relatively centered within the  
 506 range of values predicted by empirical GMPEs (either BI2014 or BSSA), there are some significant  
 507 differences in the ground-motion variability. The PGA and PGV simulated for SFSS scenarios often  
 508 deviate from the lognormal distribution commonly used to describe the ground-motion variability.  
 509 Skewed synthetic distributions are also detected, thereby showing how much directivity effects of  
 510 large events (M7.0) should be accounted for in a reliable ground motion characterization in the  
 511 near-source distance range (Figure 4 and more details of these distributions in the Electronic  
 512 Supplement of this work). The synthetic ground motion variability ( $\sigma_{DSM}$ ) of the explored scenario  
 513 events is heteroscedastic, with smaller values for larger earthquakes (Figure 6a). The GMPE  
 514 variability ( $\sigma_{GMPE}$ ), on the other hand, is linked with source, propagation, and site characteristics, as  
 515 well as earthquake data availability; the  $\sigma_{DSM}$  in our case study is linked to the modeled scenario

516 events in terms of source-to-site distance and directivity. The tails of the ground motion  
517 distributions have significant overlaps. This indicates that, although we are looking at the same fault  
518 source, it is significantly likely that ground motion levels expected for higher magnitude  
519 earthquakes could also be exceeded by smaller earthquakes.

520 From the synthetic dataset, we calibrated a set of synthetic attenuation models including directivity  
521 effects by means of the apparent stress parameter. The associated variability is reduced of more  
522 than 50% with respect to the simple model described by Eq. 3, which depends on distance only. The  
523 standard deviation of this model represents the variability of ground motion expected at a single site  
524 from a single fault, where several rupture scenarios may occur.

525 Although the proposed functional form is very simple, we do introduce an additional parameter –  
526 the apparent stress  $\Delta_{app}$  – that implies the treatment of its associated epistemic uncertainty. This is  
527 indeed a critical point in hazard assessment because the hazard levels are sensitive to the weighting  
528 scheme.

529 As a further development, the predicted ground-motion median and its related variability for the  
530 SFSS configuration can be extended to a grid of virtual receivers, using the concept of apparent  
531 stress parameter, to calibrate synthetic ground motion equations useful in different fault-to-site  
532 configurations.

533 The above considerations and results suggest that DSM simulations are accurate enough to be used  
534 in seismic hazard applications and, although they have a higher computational cost than the  
535 GMPEs, they provide an added value represented by 1) one-to-one association between seismic  
536 source characteristics and their calculated effects; 2) possibility to supply results in any hazard  
537 ground motion parameters directly derived from synthetic waveforms; 3) possibility to explore the  
538 ground motion variability due to several fault kinematic parameters, directivity, and short source-to-  
539 site distances; 4) integration with empirical ground motion models, especially for moderate-to-large  
540 magnitudes in the near-source region where recorded data are usually poor or nonexistent; 5) PSHA

541 accounting for heteroscedastic features of the ground motion; 6) total removal of the ergodic  
542 assumption for prevailing path-specific effects.

## 543 **Data and Resources**

544 Accelerometric waveforms and related metadata can be retrieved from the ITalian ACcelerometric  
545 Archive ITACA 2.0 at <http://itaca.mi.ingv.it> (last accessed May 2016); data from the DISS Working  
546 Group (2010) can be found at <http://diss.rm.ingv.it/diss/> (last accessed May 2016). Data from the  
547 Gruppo di Lavoro MPS (2004) can be found at <http://zonesismiche.mi.ingv.it> (last accessed May  
548 2016). PGAs with probability of exceedance in 50 years were calculated by using the CRISIS2015  
549 program, made by Universidad National Autónoma de México  
550 (<https://sites.google.com/site/codecrisis2015/>; last accessed May 2016). The figures in this work  
551 were mainly drawn with MATLAB and Statistics Toolbox Release 2012b, The MathWorks, Inc.,  
552 Natick, Massachusetts, United States. Information about the work in progress about the upgrading  
553 version of the current Italian seismic hazard map (MPS16) can be found at  
554 <http://tinyurl.com/jg99xsc> (in Italian, last accessed May 2016).

555

## 556 **Acknowledgments**

557 This work was supported by the project MASSIMO - Cultural Heritage Monitoring in Seismic  
558 Area, PON01/02710 - coordinated by Istituto Nazionale di Geofisica e Vulcanologia (INGV) and  
559 funded by the Italian Ministry of Education, University and Research. MMT is supported by the  
560 INGV - DPC-CPS Agreement. We thank G. Lanzano and L. Luzi for helping us in the regression  
561 analyses of the synthetic data, and G. Valensise for his support in the development of the project.  
562 The authors are also grateful to B. Bradley and two anonymous reviewers for their criticisms and  
563 suggestions, which improved the quality of this study.

564

565   **References**

- 566   Akkar, S., and J. J. Bommer (2007a). Empirical Prediction Equations for Peak Ground Velocity  
567   Derived from Strong-Motion Records from Europe and the Middle East, *B. Seismol. Soc. Am.*, **97**,  
568   511-530, doi:10.1785/0120060141.
- 569   Akkar, S., and J. J. Bommer (2007b). Prediction of elastic displacement response spectra in Europe  
570   and the Middle East, *Earthquake Engineering & Structural Dynamics*, **36**, 1275-1301,  
571   doi:10.1002/eqe.679.
- 572   Al Atik, L., N. Abrahamson, J. J. Bommer, F. Scherbaum, F. Cotton, and N. Kuehn (2010). The  
573   Variability of Ground-Motion Prediction Models and Its Components, *Seismol. Res. Lett.*, **81**, 794-  
574   801, doi:10.1785/gssrl.81.5.794.
- 575   Ambraseys, N. N., J. Douglas, S. K. Sarma, and P. M. Smit (2005). Equations for the Estimation of  
576   Strong Ground Motions from Shallow Crustal Earthquakes Using Data from Europe and the Middle  
577   East: Vertical Peak Ground Acceleration and Spectral Acceleration, *B. Earthq. Eng.*, **3**, 55-73,  
578   doi:10.1007/s10518-005-0186-x.
- 579   Ameri, G., A. Emolo, F. Pacor, and F. Gallovic (2011). Ground-Motion Simulations for the 1980 M  
580   6.9 Irpinia Earthquake (Southern Italy) and Scenario Events, *B. Seismol. Soc. Am.*, **101**, 1136-1151,  
581   doi:10.1785/0120100231.
- 582   Ameri, G., F. Gallovic, F. Pacor, and A. Emolo (2009). Uncertainties in Strong Ground-Motion  
583   Prediction with Finite-Fault Synthetic Seismograms: An Application to the 1984 M 5.7 Gubbio,  
584   Central Italy, Earthquake, *B. Seismol. Soc. Am.*, **99**, 647-663, doi:10.1785/0120080240.
- 585   Ameri, G., F. Pacor, G. Cultrera, and G. Franceschina (2008). Deterministic Ground-Motion  
586   Scenarios for Engineering Applications: The Case of Thessaloniki, Greece, *B. Seismol. Soc. Am.*,  
587   **98**, 1289-1303, doi:10.1785/0120070114.
- 588   American Society of Civil Engineers (ASCE) (2005). Minimum Design Loads for Buildings and  
589   Other Structures, (ASCE/SEI 7-05), ASCE, Reston, Virginia.



590 American Society of Civil Engineers (ASCE) (2010). Minimum Design Loads for Buildings and  
 591 Other Structures, (ASCE/SEI 7-10), ASCE, Reston, Virginia.

592 Anderson, J. G., and J. N. Brune (1999). Probabilistic Seismic Hazard Analysis without the Ergodic  
 593 Assumption, *Seismol. Res. Lett.*, **70**, 19-28, doi:10.1785/gssrl.70.1.19.

594 Anderson, J. G., and S. E. Hough (1984). A model for the shape of the Fourier amplitude spectrum  
 595 of acceleration at high frequencies, *B. Seismol. Soc. Am.*, **74**, 1969-1993.

596 Atkinson, G. M. and D. M. Boore (2006). Earthquake Ground-Motion Prediction Equations for  
 597 Eastern North America, *B. Seismol. Soc. Am.*, **96**, 2181–2205.

598 Atkinson, G. M. (2015). Ground-Motion Prediction Equation for Small-to-Moderate Events at  
 599 Short Hypocentral Distances, with Application to Induced-Seismicity Hazards, *B. Seismol. Soc.*  
 600 *Am.*, **105**, 981-992, doi:10.1785/0120140142.

601 Barberi, G., M. T. Cosentino, A. Gervasi, I. Guerra, G. Neri, and B. Orecchio (2004). Crustal  
 602 seismic tomography in the Calabrian Arc region, south Italy, *Phys. Earth Planet. In.*, **147**, 297-314,  
 603 doi:10.1016/j.pepi.2004.04.005.

604 Basili, R., G. Valensise, P. Vannoli, P. Burrato, U. Fracassi, S. Mariano, M. M. Tiberti, and E.  
 605 Boschi (2008). The Database of Individual Seismogenic Sources (DISS), version 3: Summarizing  
 606 20 years of research on Italy's earthquake geology, *Tectonophysics*, **453**, 20-43,  
 607 doi:http://dx.doi.org/10.1016/j.tecto.2007.04.014.

608 Bazzurro, P., and C. Allin Cornell (1999). Disaggregation of seismic hazard, *B. Seismol. Soc. Am.*,  
 609 **89**, 501-520.

610 Bernard, P., and R. Madariaga (1984). A new asymptotic method for the modeling of near-field  
 611 accelerograms, *B. Seismol. Soc. Am.*, **74**, 539-557.

612 Bindi, D., M. Massa, L. Luzi, G. Ameri, F. Pacor, R. Puglia, and P. Augliera (2014). Pan-European  
 613 ground-motion prediction equations for the average horizontal component of PGA, PGV, and 5 %-

614 damped PSA at spectral periods up to 3.0 s using the RESORCE dataset, *B. Earthq. Eng.*, **12**, 391-  
615 430, doi:10.1007/s10518-013-9525-5.

616 Bommer, J. J. (2002). Deterministic Vs. Probabilistic Seismic Hazard Assessment: An Exaggerated  
617 and Obstructive Dichotomy, *J. Earthq. Eng.*, **6**, 43-73, doi:10.1080/13632460209350432.

618 Bommer, J. J., and N. A. Abrahamson (2006). Why Do Modern Probabilistic Seismic-Hazard  
619 Analyses Often Lead to Increased Hazard Estimates?, *B. Seismol. Soc. Am.*, **96**, 1967-1977,  
620 doi:10.1785/0120060043.

621 Bommer, J. J., P. J. Stafford, J. E. Alarcon, and S. Akkar (2007). The Influence of Magnitude  
622 Range on Empirical Ground-Motion Prediction, *B. Seismol. Soc. Am.*, **97**, 2152-2170,  
623 doi:10.1785/0120070081.

624 Boore, D. M. (1983). Stochastic simulation of high-frequency ground motions based on  
625 seismological models of the radiated spectra, *B. Seismol. Soc. Am.*, **73**, 1865-1894.

626 Boore, D. M. (2003). Simulation of Ground Motion Using the Stochastic Method, *Pure Appl.*  
627 *Geophys.*, **160**, 635-676, doi:10.1007/PL00012553.

628 Boore, D. M., and W. B. Joyner (1997). Site amplifications for generic rock sites, *B. Seismol. Soc.*  
629 *Am.*, **87**, 327-341.

630 Boore, D. M., J. P. Stewart, E. Seyhan, and G. M. Atkinson (2014). NGA-West2 Equations for  
631 Predicting PGA, PGV, and 5% Damped PSA for Shallow Crustal Earthquakes, *Earthquake Spectra*,  
632 **30**, 1057-1085, doi:10.1193/070113eqs184m.

633 Brune. J.N., (1970). Tectonic stress and the spectra of seismic shear waves from earthquakes. *J.*  
634 *Geophys. Res.*, **75**, 4997–5009.

635 Building Seismic Safety Council (BSSC) (2009). NEHRP Recommended Seismic Provisions for  
636 New Buildings and Other Structures, (FEMA P-750), prepared for the Federal Emergency  
637 Management Agency, Washington, DC.

638 Carafa, M. M. C., and S. Barba (2013). The stress field in Europe: optimal orientations with  
639 confidence limits, *Geophys. J. Int.*, **193**, 531-548, doi:10.1093/gji/ggt024.

640 Carvalho, A., G. Zonno, G. Franceschina, J. Bilé Serra, and A. Campos Costa (2008). Earthquake  
641 shaking scenarios for the metropolitan area of Lisbon, *Soil Dyn. Earthq. Eng.*, **28**, 347-364,  
642 doi:10.1016/j.soildyn.2007.07.009.

643 Chapman, M. C. (1995). A probabilistic approach to ground-motion selection for engineering  
644 design, *B. Seismol. Soc. Am.*, **85**, 937-942.

645 Convertito, V. (2006). Seismic-Hazard Assessment for a Characteristic Earthquake Scenario: An  
646 Integrated Probabilistic-Deterministic Method, *B. Seismol. Soc. Am.*, **96**, 377-391,  
647 doi:10.1785/0120050024.

648 Cultrera, G., A. Cirella, E. Spagnuolo, A. Herrero, E. Tinti, and F. Pacor (2010). Variability of  
649 Kinematic Source Parameters and Its Implication on the Choice of the Design Scenario, *B. Seismol.*  
650 *Soc. Am.*, **100**, 941-953, doi:10.1785/0120090044.

651 D'Amico, S., B. Orecchio, D. Presti, A. Gervasi, L. Zhu, I. Guerra, G. Neri, and R. Herrmann  
652 (2011). Testing the stability of moment tensor solutions for small earthquakes in the Calabro-  
653 Peloritan Arc region (southern Italy), *Boll. Geof. Teor. Appl.*, **52**, 283-298, doi:10.4430/bgta0009.

654 DISS Working Group (2010). Database of Individual Seismogenic Sources (DISS), Version 3.1.1:  
655 A compilation of potential sources for earthquakes larger than M 5.5 in Italy and surrounding areas.  
656 <http://diss.rm.ingv.it/diss/>, Istituto Nazionale di Geofisica e Vulcanologia; DOI:10.6092/INGV.IT-  
657 DISS3.1.1.

658 Dreger, D. S., and T. H. Jordan (2015). Introduction to the Focus Section on Validation of the  
659 SCEC Broadband Platform V14.3 Simulation Methods, *Seismol. Res. Lett.*, **86**, 15-16,  
660 doi:10.1785/0220140233.

661 Ericson, C. A. (2005). Hazard analysis techniques for system safety, John Wiley & Sons.

662 Faccioli, E. (2013). Recent evolution and challenges in the Seismic Hazard Analysis of the Po Plain  
663 region, Northern Italy, *B. Earthq. Eng.*, **11**, 5-33, doi:10.1007/s10518-012-9416-1.

664 Goulet, C. A., Abrahamson, N. A., Somerville, P. G., & Wooddell, K. E. (2015). The SCEC  
665 Broadband Platform Validation Exercise: Methodology for Code Validation in the Context of  
666 Seismic-Hazard Analyses. *Seismol. Res. Lett.*, **86**, 17-26. doi: 10.1785/0220140104.

667 Graves, R., T. H. Jordan, S. Callaghan, E. Deelman, E. Field, G. Juve, C. Kesselman, P. Maechling,  
668 G. Mehta, K. Milner, D. Okaya, P. Small, and K. Vahi (2010). CyberShake: A Physics-Based  
669 Seismic Hazard Model for Southern California, *Pure Appl. Geophys.*, **168**, 367-381,  
670 doi:10.1007/s00024-010-0161-6.

671 Gruppo di Lavoro MPS (2004). Redazione della mappa di pericolosità sismica prevista  
672 dall'Ordinanza PCM del 20 marzo 2003 n. 3274, All. 1. Rapporto conclusivo per il Dipartimento  
673 della Protezione Civile, aprile 2004, Istituto Nazionale di Geofisica e Vulcanologia (INGV),  
674 Milano-Roma, Italy, available at <http://zonesismiche.mi.ingv.it/> (last accessed May 2015), 163 pp.  
675 (in Italian).

676 Hanks, T. C., and H. Kanamori (1979). A moment magnitude scale, *J. Geophys. Res.*, **84**, 2348,  
677 doi:10.1029/JB084iB05p02348.

678 International Atomic Energy Agency (IAEA) (2002). Evaluation of seismic hazards for nuclear  
679 power plants: safety guide, IAEA Safety standards series, ISSN 1020–525X; no. NS-G-3.3, IAEA,  
680 Vienna.

681 International Atomic Energy Agency (IAEA) (2010). Seismic hazard in site evaluation for nuclear  
682 installations: safety guide. IAEA safety standards series, ISSN 1020-525X; no. SSG-9, IAEA,  
683 Vienna.

684 Kanamori, H., and D. L. Anderson (1975). Theoretical basis of some empirical relations in  
685 seismology, *B. Seismol. Soc. Am.*, **65**, 1073-1095.

686 Locati, M., R. Camassi, and M. E. Stucchi (2011). DBMI11, la versione 2011 del Database

687 Macrosismico Italiano. Milano, Bologna, <http://emidius.mi.ingv.it/DBMI11>, DOI:  
688 10.6092/INGV.IT-DBMI11.

689 Lorito, S., J. Selva, R. Basili, F. Romano, M. M. Tiberti, and A. Piatanesi (2015). Probabilistic  
690 hazard for seismically induced tsunamis: accuracy and feasibility of inundation maps, *Geophys. J.*  
691 *Int.*, **200**, 574-588, doi:10.1093/gji/ggu408.

692 Luzi, L., D. Bindi, R. Puglia, F. Pacor, and A. Oth (2014). Single-Station Sigma for Italian  
693 Strong-Motion Stations, *B. Seismol. Soc. Am.*, doi:10.1785/0120130089.

694 Luzi, L., S. Hailemichael, D. Bindi, F. Pacor, F. Mele, and F. Sabetta (2008). ITACA (ITalian  
695 ACcelerometric Archive): A Web Portal for the Dissemination of Italian Strong-motion Data,  
696 *Seismol. Res. Lett.*, **79**, 716-722, doi:10.1785/gssrl.79.5.716.

697 Martinelli, F., and C. Meletti (2008). A WebGIS Application for Rendering Seismic Hazard Data in  
698 Italy, *Seismol. Res. Lett.*, **79**, 68-78, doi:10.1785/gssrl.79.1.68.

699 Marzocchi, W., M. Taroni, and J. Selva (2015). Accounting for epistemic uncertainty in PSHA:  
700 Logic Tree and ensemble modeling, *B. Seismol. Soc. Am.*, **105**(4), 2151–2159.

701 McGuire, R. K. (1995). Probabilistic seismic hazard analysis and design earthquakes: Closing the  
702 loop, *B. Seismol. Soc. Am.*, **85**, 1275-1284.

703 McGuire, R. K. (2001). Deterministic vs. probabilistic earthquake hazards and risks, *Soil Dyn.*  
704 *Earthq. Eng.*, **21**, 377-384, doi:10.1016/S0267-7261(01)00019-7.

705 Meletti, C., G. M. Calvi, and M. Stucchi (2007). Progetto S1: proseguimento della assistenza al  
706 DPC per il completamento e la gestione della mappa di pericolosità sismica prevista dall'Ordinanza  
707 PCM 3274/2003 e progettazione di ulteriori sviluppi, DPC-INGV S1 Project, Final Report,  
708 available at [http://esse1.mi.ingv.it/data/S1\\_Rendicontazione\\_Scientifica\\_finale\\_S1.pdf](http://esse1.mi.ingv.it/data/S1_Rendicontazione_Scientifica_finale_S1.pdf)

709 Meletti, C., F. Galadini, G. Valensise, M. Stucchi, R. Basili, S. Barba, G. Vannucci, and E. Boschi  
710 (2008). A seismic source zone model for the seismic hazard assessment of the Italian territory,

711 *Tectonophysics*, **450**, 85-108, doi:10.1016/j.tecto.2008.01.003.

712 Motazedian, D. and G. M. Atkinson (2005). Stochastic finite-fault modeling based on a dynamic  
713 corner frequency. *B. Seismol. Soc. Am.*, **95**, 995–1010.

714 Mualchin, L. (1996). A technical report to accompany the CALTRANS California seismic hazard  
715 map 1996 (based on maximum credible earthquakes), California Department of Transportation  
716 Engineering Service Center.

717 Newhall, C., and R. Hoblitt (2002). Constructing event trees for volcanic crises, *B. Volcanol.*, **64**, 3-  
718 20, doi:10.1007/s004450100173.

719 Ordaz, M., F. Martinelli, V. D'Amico, and C. Meletti (2013). CRISIS2008: A Flexible Tool to  
720 Perform Probabilistic Seismic Hazard Assessment, *Seismol. Res. Lett.*, **84**, 495-504,  
721 doi:10.1785/0220120067.

722 Orecchio, B., D. Presti, C. Totaro, I. Guerra, and G. Neri (2011). Imaging the velocity structure of  
723 the Calabrian Arc region (southern Italy) through the integration of different seismological data,  
724 *Boll. Geof. Teor. Appl.*, **52**, 625-638, doi:10.4430/bgta0023.

725 Pacor, F., G. Cultrera, A. Mendez, and M. Cocco (2005). Finite Fault Modeling of Strong Ground  
726 Motions Using a Hybrid Deterministic-Stochastic Approach, *B. Seismol. Soc. Am.*, **95**, 225-240,  
727 doi:10.1785/0120030163.

728 Pacor, F., R. Paolucci, L. Luzi, F. Sabetta, A. Spinelli, A. Gorini, M. Nicoletti, S. Marcucci, L.  
729 Filippi, and M. Dolce (2011). Overview of the Italian strong motion database ITACA 1.0, *B.*  
730 *Earthq. Eng.*, **9**, 1723-1739, doi:10.1007/s10518-011-9327-6.

731 Parolai, S., and D. Bindi (2004). Influence of Soil-Layer Properties on k Evaluation, *B. Seismol.*  
732 *Soc. Am.*, **94**, 349-356, doi:10.1785/0120030022.

733 Restrepo-Velez, L. F., and J. J. Bommer (2003). An exploration of the nature of the scatter in  
734 ground-motion prediction equations and the implications for seismic hazard assessment. *Journal of*

735 Earthquake Engineering, **7**, 171–199. [doi.org/10.1142/S1363246903001000](https://doi.org/10.1142/S1363246903001000)

736 Rovelli, A., O. Bonamassa, M. Cocco, M. Di Bona, and S. Mazza (1988). Scaling laws and spectral  
 737 parameters of the ground motion in active extensional areas in Italy, *B. Seismol. Soc. Am.*, **78**, 530-  
 738 560.

739 Rovida, A., R. Camassi, P. Gasperini, and M. e. Stucchi (2011). CPTI11, the 2011 version of the  
 740 Parametric Catalogue of Italian Earthquakes. Istituto Nazionale di Geofisica e Vulcanologia,  
 741 Milano, Bologna.DOI: <http://doi.org/10.6092/INGV.IT-CPTI11>.

742 Ruiz-García, J. (2011). Inelastic Displacement Ratios for Seismic Assessment of Structures  
 743 Subjected to Forward-Directivity Near-Fault Ground Motions, *J. Earthq. Eng.*, **15**, 449-468,  
 744 doi:10.1080/13632469.2010.498560.

745 Selva J., Tonini R., Molinari I., Tiberti M.M., Romano F., Grezio A., Melini D., Piatanesi A., Basili  
 746 R., Lorito S. (2016). Quantification of source uncertainties in Seismic Probabilistic Tsunami Hazard  
 747 Analysis (SPTHA). *Geophys. J. Int.*, 205, 1780-1803, doi:10.1093/gji/ggw107.

748 Spudich, P., and L. N. Frazer (1984). Use of ray theory to calculate high-frequency radiation from  
 749 earthquake sources having spatially variable rupture velocity and stress drop, *B. Seismol. Soc. Am.*,  
 750 **74**, 2061-2082.

751 Strasser, F., J. Bommer, and N. Abrahamson (2008). Estimating ground-motion variability: issues,  
 752 insights & challenges, in *The 14<sup>th</sup> World Conference on Earthquake Engineering, October 12-17,*  
 753 *2008, Beijing, China.*

754 Stucchi, M., C. Meletti, V. Montaldo, H. Crowley, G. M. Calvi, and E. Boschi (2011). Seismic  
 755 Hazard Assessment (2003–2009) for the Italian Building Code, *B. Seismol. Soc. Am.*, **101**, 1885-  
 756 1911, doi:10.1785/0120100130.

757 Villani, M., and N. A. Abrahamson (2015). Repeatable site and path effects on the ground-motion  
 758 sigma based on empirical data from southern California and simulated waveforms from the

759 CyberShake platform. *B. Seismol. Soc. Am.*, doi:10.1785/0120140359

760 Villani, M., E. Faccioli, M. Ordaz, and M. Stupazzini (2014). High-Resolution Seismic Hazard

761 Analysis in a Complex Geological Configuration: The Case of the Sulmona Basin in Central Italy,

762 *Earthquake Spectra*, **30**, 1801-1824, doi:10.1193/1112911eqs288m.

763 Yagoda-Biran, G., J. G. Anderson, H. Miyake, and K. Koketsu (2015). Between-Event Variance

764 for Large Repeating Earthquakes, *B. Seismol. Soc. Am.*, **105**, 2023-2040, doi:10.1785/0120140196.

765



766 **Full mailing address for each author**

767

768 Maria D'Amico and Francesca Pacor

769 Istituto Nazionale di Geofisica e Vulcanologia, Sezione di Milano, Via Corti 12, 20133, Milano,

770 Italy.

771

772 Mara Monica Tiberti and Roberto Basili

773 Istituto Nazionale di Geofisica e Vulcanologia, Sezione di Roma1, Via di Vigna Murata 605, 00143

774 Roma, Italy

775

776 Emiliano Russo

777 Istituto Nazionale di Geofisica e Vulcanologia, Centro Nazionale Terremoti, Via di Vigna Murata

778 605, 00143 Roma, Italy

779

780 **Tables**  
781

**Table 1**  
Modeling parameters for the simulations at Cosenza

Parameter	Value
Strike, Dip, Rake [°]	180, 60, 270
Shear-wave velocity [km/s] ( $\beta$ )	3.4 <sup>1</sup> , 3.4 <sup>2</sup> , 2.5 <sup>3</sup> , 2.7 <sup>4</sup> , 3.5 <sup>5</sup>
Density [g/cm <sup>3</sup> ]	2.6 <sup>1</sup> , 2.5 <sup>2</sup> , 2.5 <sup>3</sup> , 2.5 <sup>4</sup> , 2.6 <sup>5</sup>
Rupture propagation speed [km/s] ( $V_r$ )	0.7, 0.8, 0.85 ( $\times \beta$ )
$K_0$ [s]	0.02, 0.025, 0.035
Geometric spreading	1/R
Quality factor ( $Q_s$ )	100

Average shear-wave velocity, crustal density and rupture velocity depend on the fault size and depth (see Table 2): <sup>1</sup> M7.0 (1-30 km); <sup>2</sup> M6.0 (1-15 km); <sup>3</sup> M5.0 (1-3.3 km); <sup>4</sup> M5.0 (5-7.3 km); <sup>5</sup> M5.0 (7-9.3 km).  $Q_s$  is from Rovelli et al. (1988).

782  
783

**Table 2**  
Fault-rupture parameters of Child Faults and source-to-site distance range

$M_w$	Length [km]	Width [km]	Top Depth [km]	Bottom Depth [km]	$M_0$ [Nm]	Mean slip [m]	$R_{JB}$ or $R_{epi}$ [km]
<b>7.0</b>	37.0	26.0	1.0	23.5	$4.0 \times 10^{19}$	1.40	0
<b>6.0</b>	13.0	9.0	1.0	8.8	$1.4 \times 10^{18}$	0.40	0 - 7
<b>5.0</b>	4.0	2.7	1,5,7	3.3,7.3,9.3	$4.2 \times 10^{16}$	0.13	0 – 15*

\* Epicentral distance.

784  
785  
786

**Table 3**  
Number of shaking scenarios performed for the city of Cosenza for each magnitude

M	#Nucleation Point	#rupture velocity	# $k_0$	#modeled faults	#simulations
<b>7.0</b>	27	3	3	1	243
<b>6.0</b>	9	3	3	5	405
<b>5.0</b>	3	3	3	23	621

787  
788

789  
790

**Table 4**  
Crustal velocity model

Depth [km]	Vp [km/s]	Vs [km/s]	ρ [g/cm <sup>3</sup> ]
0	4.50	2.49	2.50
5	5.00	2.76	2.50
8	6.00	3.31	2.60
15	6.50	3.59	2.70
18	6.80	3.76	2.80
30	7.50	4.14	2.90
40	7.50	4.76	2.90

Data from (Barberi et al., 2004; Orecchio et al., 2011;  
D’Amico et al., 2011). Vs = Vp/1.81 (km/s).

791  
792  
793

**Table 5**  
Summary of PGA and PGV values

	M	R <sub>JB</sub>	BI2014	BSSA	M1	M2	M3
PGA [cm/s <sup>2</sup> ]	7.0	0	2.60	2.49	2.58-2.59*	2.66-2.67*	2.68-2.56*
	6.0	0	2.41	2.44	2.34	2.47	2.53
	6.0	5	2.26	2.28	2.06	2.22	2.30
	5.0	5	1.98	1.91	2.00	1.95	2.07
	5.0	10	1.65	1.62	1.75	1.71	1.85
PGV [cm/s]	7.0	0	1.62	1.49	1.51-1.49*	1.60-1.56*	1.61-1.65*
	6.0	0	1.23	1.20	1.17	1.28	1.34
	6.0	5	1.08	1.06	0.88	1.02	1.10
	5.0	5	0.57	0.42	0.68	0.63	0.73
	5.0	10	0.24	0.15	0.41	0.38	0.59

PGA and PGV medians of empirical models are derived from BSSA (Boore et al., 2014) and BI2014 (Bindi et al., 2014) for each magnitude-distance bin considered in this work. Corresponding PGA and PGV synthetic values (log10 units) are derived from simulations at the target site (CSZ) considering the three different scenario model configurations (M1, M2, and M3 combined with the DSM local metric); \* values for the quasi-unilateral site (s001).

**Table 6**  
Summary of PGA and PGV variability

IMT	M	R <sub>JB</sub>	BSSA			BI2014			M1	M2	M3
			$\sigma$	$\phi$	$\tau$	$\sigma$	$\phi$	$\tau$	$\sigma_{\text{DSM}}$	$\sigma_{\text{DSM}}$	$\sigma_{\text{DSM}}$
PGA	7.0	0	0.27	0.22	0.15				0.17-0.18*	0.11-0.16*	0.13-0.10*
	6.0	0	0.27	0.22	0.15				0.27	0.10	0.14
	6.0	5	0.27	0.22	0.15	0.33	0.28	0.18	0.35	0.09	0.16
	5.0	5	0.31	0.27	0.16				0.37	0.23	0.33
	5.0	10	0.31	0.27	0.16				0.38	0.20	0.30
PGV	7.0	0	0.28	0.24	0.15				0.15-0.16*	0.09-0.14*	0.13-0.10*
	6.0	0	0.28	0.24	0.15				0.22	0.06	0.10
	6.0	5	0.28	0.24	0.15	0.33	0.27	0.19	0.30	0.06	0.13
	5.0	5	0.31	0.26	0.16				0.35	0.24	0.32
	5.0	10	0.31	0.26	0.16				0.33	0.20	0.27

PGA and PGV variability derived from BSSA (Boore et al., 2014) and BI2014 (Bindi et al., 2014) empirical models for each magnitude-distance considered in this work (log10 units):  $\sigma$ ) empirical total standard deviation;  $\Phi$ ) within-event component of the empirical total standard deviation;  $\tau$ ) between-event component of the total standard deviation. The corresponding standard deviation  $\sigma_{\text{DSM}}$  of the synthetic statistical distributions are also reported. The ground motion was simulated at the target site (CSZ) considering the three different scenario model configurations (M1, M2, and M3 combined with the DSM local metric); values denoted by \* are for the quasi-unilateral site (s001).

800

**Table 7**  
Summary of the regression results for each simulation method setup and  
sampled magnitude (M): first step

Setup	c <sub>1</sub>	c <sub>2</sub>	h <sub>eff</sub>	d	σ <sub>reg</sub>	M
GM-M1	1.14	-2.26	7.32	30	0.37	5.0
	1.56	-1.39	7.32	34	0.39	6.0
	1.60	-2.40	19	64	0.19	7.0
GM-M2	1.14	-2.15	7.32	30	0.14	5.0
	1.56	-1.78	7.32	34	0.16	6.0
	1.60	-2.62	19	64	0.11	7.0
GM-M3	1.14	-2.51	7.32	30	0.30	5.0
	1.56	-1.89	7.32	34	0.26	6.0
	1.60	-2.66	19	64	0.13	7.0

Legend: c<sub>1</sub> and c<sub>2</sub>, regression coefficients; h<sub>eff</sub>, effective depth; d, joint  
distance; and σ<sub>reg</sub>, standard deviation of the empirical residuals (log10 units).

801

802

803

**Table 8**  
Summary of the regression results for each sampled  
magnitude (M) and for M1 model setup: second step

Setup	c <sub>3</sub>	c <sub>4</sub>	σ*	M
GM-M1	-1.21	0.81	0.13	5.0
	-0.99	0.83	0.11	6.0
	-1.35	1.00	0.10	7.0

Legend: c<sub>3</sub> and c<sub>4</sub>, regression coefficients; σ\*, standard  
deviation of the empirical residuals (log10 units).

804

805

## 806 List of Figure Captions

807 **Figure 1.** a) Seismic hazard map of the Cosenza broader region. Contours represent horizontal peak  
808 ground acceleration (PGA) with 10% probability of exceedance in 50 years on hard ground (values  
809 expressed as multiples of g; PGA contour interval is of 0.025 g) from MPS04 (Meletti et al., 2007).  
810 The black rectangle outlines the M7.0 fault source. White triangle and white star show the location  
811 of target sites CSZ and s001, respectively. Grey dots are historical earthquakes with  $M_w \geq 5.0$  from  
812 CPTI11 (Rovida et al., 2011). b) Sketch of the simulated fault planes for each magnitude (M7.0,  
813 M6.0, and M5.0). The position of target sites relative to the faults is also shown; symbols as in  
814 panel a). c) Stem plot of the Cosenza's seismic history from DBMI11 (Locati et al., 2011). d)  
815 Disaggregation plot (interpolated) from MPS04 for Cosenza for the source-to-site distance range of  
816 0-10 km (Meletti et al., 2007; Martinelli and Meletti, 2008; Stucchi et al., 2011).

817 **Figure 2.** Flow chart of the simplified event tree (ET) for sampling SFSS scenarios (see text for  
818 explanations).

819 **Figure 3.** Stresses drop variability (a) and local vs hypocentral distance (b) for each simulated  
820 magnitude (M7.0, M6.0, and M5.0) and for the simulation method setup accounting for maximum  
821 directivity effects (M1).

822 **Figure 4.** Box plots of the synthetic PGA (top) and PGV (bottom) distributions for each sampled  
823 magnitude. Each plot represents the statistical distribution of the synthetic IMTs (geometrical mean  
824 of the horizontal components) calculated for three different scenario setups: M1) apparent corner  
825 frequency; M2) standard corner frequency defined by a theoretical stress drop of 30 bars; M3)  
826 merging between M1 and M2 models based on a threshold for the apparent corner frequency  
827 corresponding to the theoretical stress drop of 30 bars. Simulations for  $M_w=7.0$  ( $R_{JB} = 0$  km) were  
828 performed both for the bilateral CSZ site and the quasi-unilateral s001 site by using the DSM local  
829 metric to define the geometrical spreading coefficient. For lower magnitudes the PGA and PGV are  
830 combined into distance groups as follows:  $R_1 = 0$  km and  $R_2 = 5$  km (Joyner-Boore distance) for

831  $M_w = 6.0$ ,  $R_1 = 5$  km and  $R_2 = 10$  km (epicentral distance) for  $M_w = 5.0$ . Each box encloses 50% of  
832 the data with the median value of the parameters represented by a horizontal line; the top and the  
833 bottom of the box mark the limits of  $\pm 25\%$  of the population; the lines extending from the top and  
834 the bottom of each box mark the minimum and the maximum values of the data; data with values  
835 1.5 times greater/lower than the top/bottom value of the box are outliers (grey cross).

836 **Figure 5.** PGAs parametric variability of the modeling setup accounting for maximum directivity  
837 effects (M1) for each simulated magnitude (M7.0, M6.0, and M5.0). a) CDFs are computed  
838 grouping scenarios events that share the same rupture velocity considering the three selected values  
839 for M6.0 and M7.0 and three different range of values for M5.0; scenarios at M5.0 and M6.0 are for  
840 distance group  $R_2 = 5$  km and  $R_2 = 10$  km, respectively (see caption of Figure 4). b) CDFs are  
841 computed grouping scenarios that share the same  $k_0$  values; c) CDFs are computed grouping  
842 scenarios that share the same rupture nucleation area considering the three sectors of the M7.0 fault  
843 (i.e. sector 1 contains nucleation points from the northern sector of the M7.0 fault). For M5.0  
844 nucleation point located into the top (TOP) or the bottom (BTM) of the M7.0 fault are also  
845 considered. All CDFs are compared to the overall distribution of the PGAs (black lines).

846

847 **Figure 6.** a) Comparison among PGA median values, along with their standard deviations, obtained  
848 for each magnitude-distance pair by DSM simulations (circles) and empirical ground motion  
849 models (triangles). The standard deviation for the empirical models are reduced by the fault-  
850 variance  $\tau^2/2$  instead of the between-event variance  $\tau$  (Yagoda-Biran et al., 2015). b) Probability  
851 Density Functions (PDFs) of the PGA ( $\text{cm/s}^2 \log_{10}$  units) synthetic distributions computed by DSM  
852 local metric at the bilateral (left) and unilateral (right) site for M7.0. The PDFs defined by three  
853 different simulation setups (M1, M2 and M3) are compared with empirical PDFs predicted by  
854 BI2014 (Bindi et al., 2014) and BSSA (Boore et al., 2014); black line: apparent corner frequency  
855 finite-fault model (M1); grey line: point-source model (M2); light-grey line: merging between M1  
856 and M2 models based on a corner frequency threshold (0.07 Hz). Empirical PDFs are plotted



857 considering the fault variance defined in Yagoda-Biran et al. (2015) as  $(\tau^2/2)$  instead of the  
858 between-event variance; the sigma estimated for a single seismic source (ABR) by Luzi et al.  
859 (2014) is also considered.

860 **Figure 7.** Comparison between BI2014 (grey lines) and synthetic PGA (black lines) ground motion  
861 models (normal faulting and EC8 soil class A), obtained by modeling a PF very close to the CSZ  
862 site. The attenuation curves inferred by regression of synthetic ground motion are for three setups of  
863 the simulation method (DSM, Pacor et al., 2005), which account for differently weighted directivity  
864 effects: maximum level (M1 top panel), minimum level (M2 central panel), and middle level (M3  
865 bottom panel). The hybrid models are obtained by adjusting BI2014 (Bindi et al., 2014) in near-  
866 source ranges at different magnitudes: M5.0 (left), M6.0 (center), and M7.0 (right). White dots  
867 represent the synthetic PGA; grey-shaded areas represent the ranges of hypocentral distances for  
868 which the empirical model and synthetic data are merged. Grey dotted lines represent the total  
869 standard deviation of the host empirical model (BI2014); light-grey lines show the sigma reduced  
870 by the fault variance  $\tau^2/2$  instead of the between-event variance  $\tau$  (GMPE-R).

871 **Figure 8.** Hybrid model total residuals for M7.0 (M1 setup) as a function of the apparent stress  
872 parameter ( $\Delta_{app}$ ) at the first (a) and second (b) steps of the regression. Residuals are calculated as  
873 synthetic PGAs minus PGAs predicted by the hybrid attenuation model ( $\log_{10}PGA_{syn} -$   
874  $\log_{10}PGA_{hyb}$ ). The dotted line (a) represents the fitting of the synthetic ground motion after  
875 correcting the median value by the directivity term due to the modeling variability of  $\Delta_{app}$ ; the grey  
876 rectangle marks the 16<sup>th</sup> and the 84<sup>th</sup> percentiles of the  $\Delta_{app}$  distribution.

877

878 **Figure 9.** PGAs hybrid ground motion models inferred by the regression of synthetic ground  
879 motion (M1 setup) and corrected for the directivity term for each magnitude (M5.0, M6.0, and  
880 M7.0). Attenuation curves are for the 16<sup>th</sup>, 50<sup>th</sup>, and 84<sup>th</sup> percentiles of the apparent stress parameter  
881 distributions.

882

883 **Figure 10.** a) Map of the ZS9 seismogenic zones (Meletti et al. 2008) in the Calabria region. The  
884 black triangle represents the city of Cosenza (CSZ), the zone with the black outline is the AS929  
885 from ZS9, used for PSHA computation, and the dash-outlined rectangle is the PF simulated in this  
886 work; b) diagram showing the cumulative (open circles) and interval (solid diamonds) seismicity  
887 rates for the GR and AR branches of MPS04 for AS929 (Gruppo di Lavoro MPS, 2004). All rates  
888 are normalized to 100 years. AS929 is characterized by an FMD with the following parameters:  $a =$   
889  $0.39$  cumulative n. eqs/yr (C. Meletti, *pers. comm.*) with reference to the minimum threshold  
890 magnitude considered ( $M_{wmin}=4.76$ );  $b = 0.82$ ; and maximum moment magnitude  $M_{wmax} = 7.29$   
891 (Stucchi et al., 2011). In the hazard calculation the  $a$ -value was appropriately reduced in order to  
892 account for a number of earthquakes coherent with the effective dimension of the modeled  
893 seismogenic source.

894 **Figure 11.** a) Annual probability of exceedance for PGA calculated at the site of interest by using  
895 empirical (black lines) or hybrid ground motion models (grey lines); b) hazard curves for a set of  
896 logic tree weights that differently combine directivity effects into M1 modeling setup. The  
897 computation of the hazard curves for empirical models was performed considering: i) the total  
898 standard deviation of the host GMPE (BI2014); ii) the sigma reduced by the fault variance  $\tau^2/2$   
899 instead of the between-event variance  $\tau$  (BI2014-R); iii) the hybrid models accounting for distinct  
900 medians and variances of the synthetic ground motion (GM-M1, GM-M2, and GM-M3); iv) the  
901 three different weights for 16<sup>th</sup>, 50<sup>th</sup> and 84<sup>th</sup> percentiles of  $\Delta_{app}$  are, respectively: WH1= 0.4, 0.5,  
902 0.1; WH2 = 0.3, 0.3, 0.3 and WH3=0.1, 0.5, 0.4.

903  
904  
905

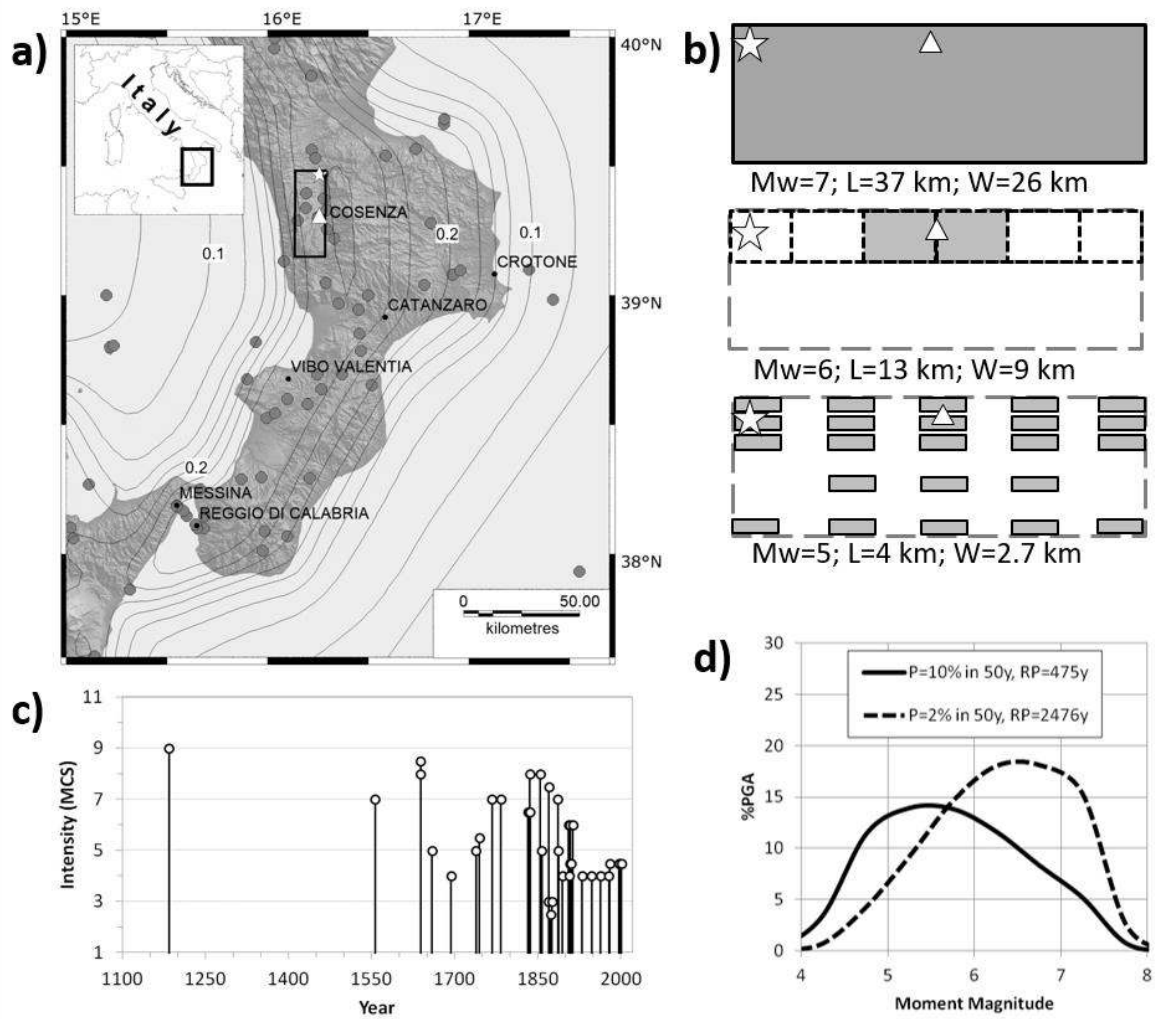


**Figure 1**

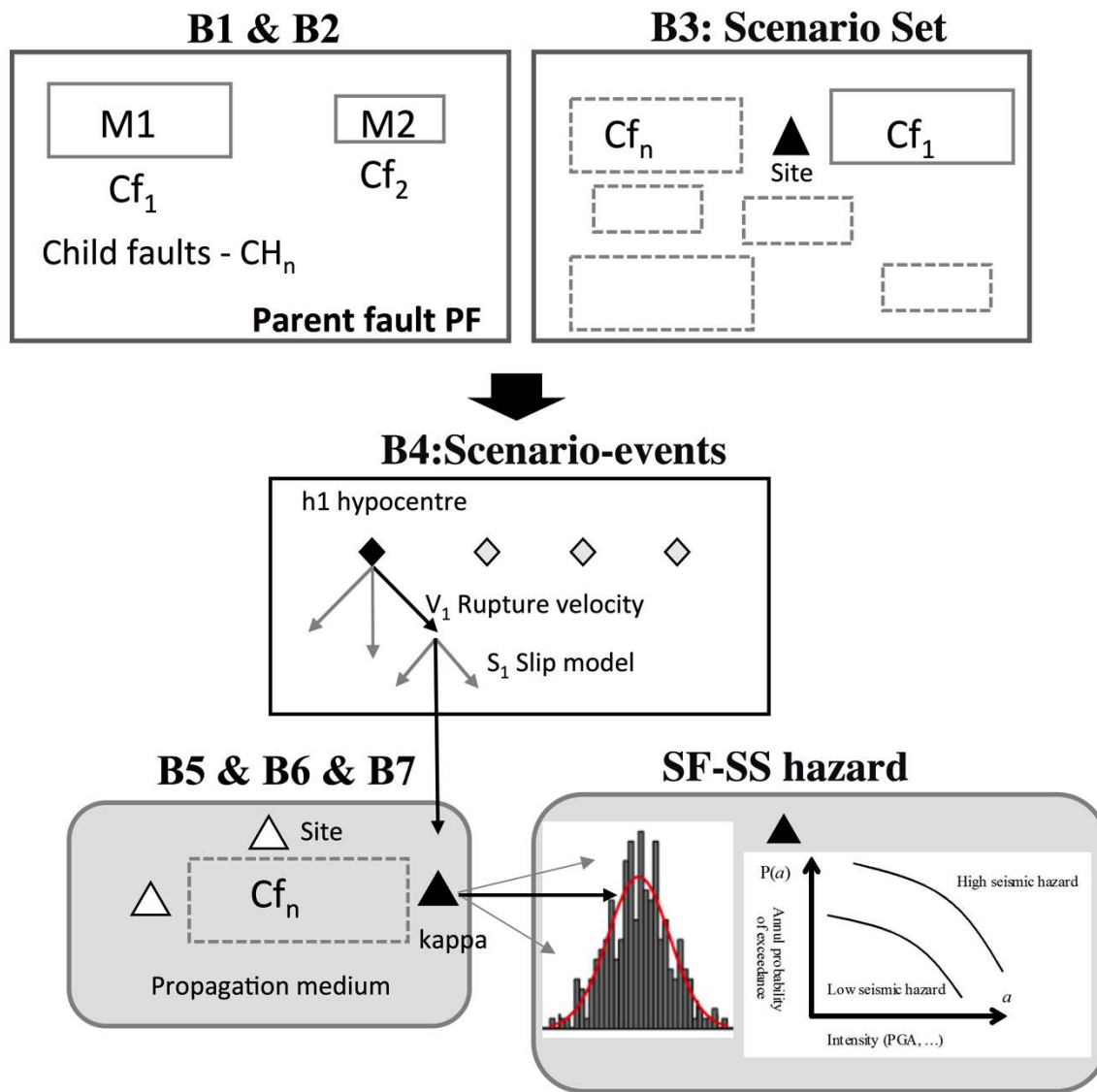


**Figure 2**

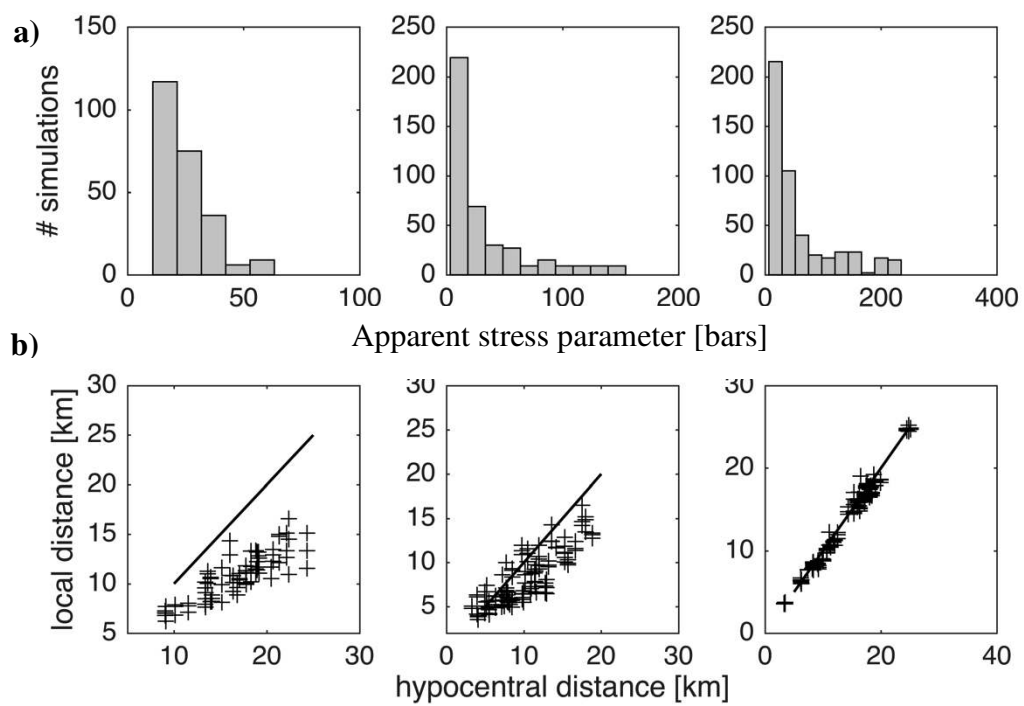
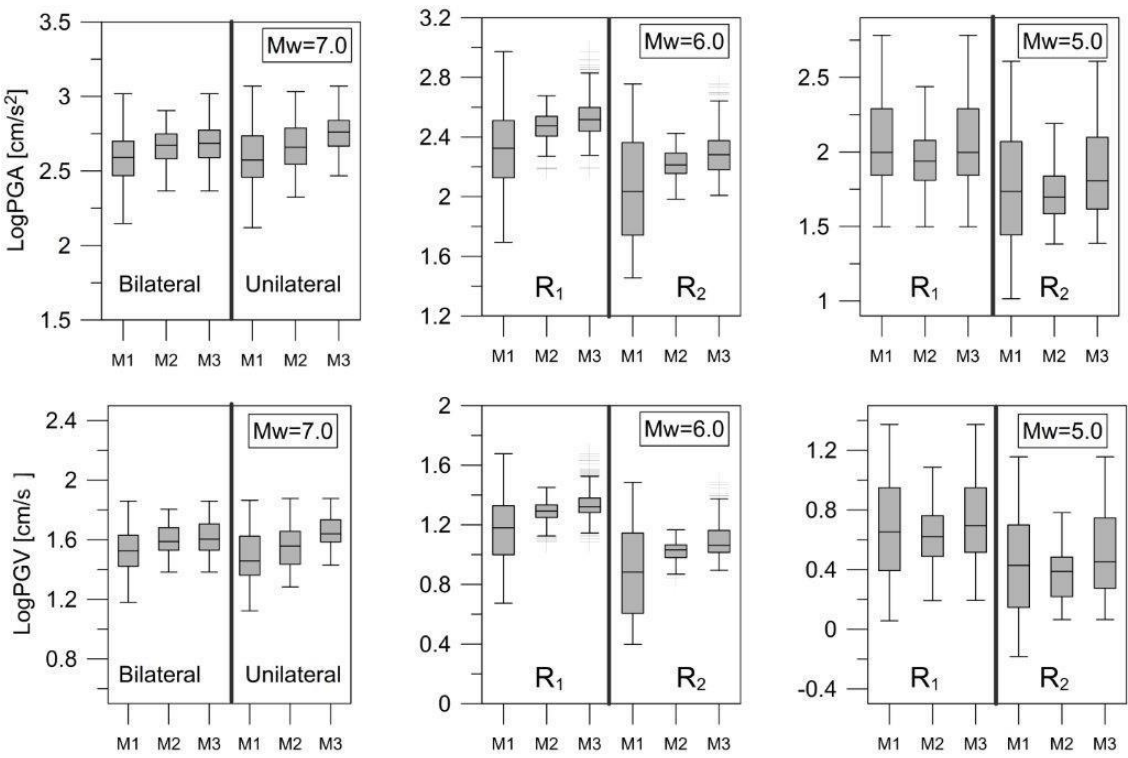


**Figure 3**

916



917

918

Figure 4

919

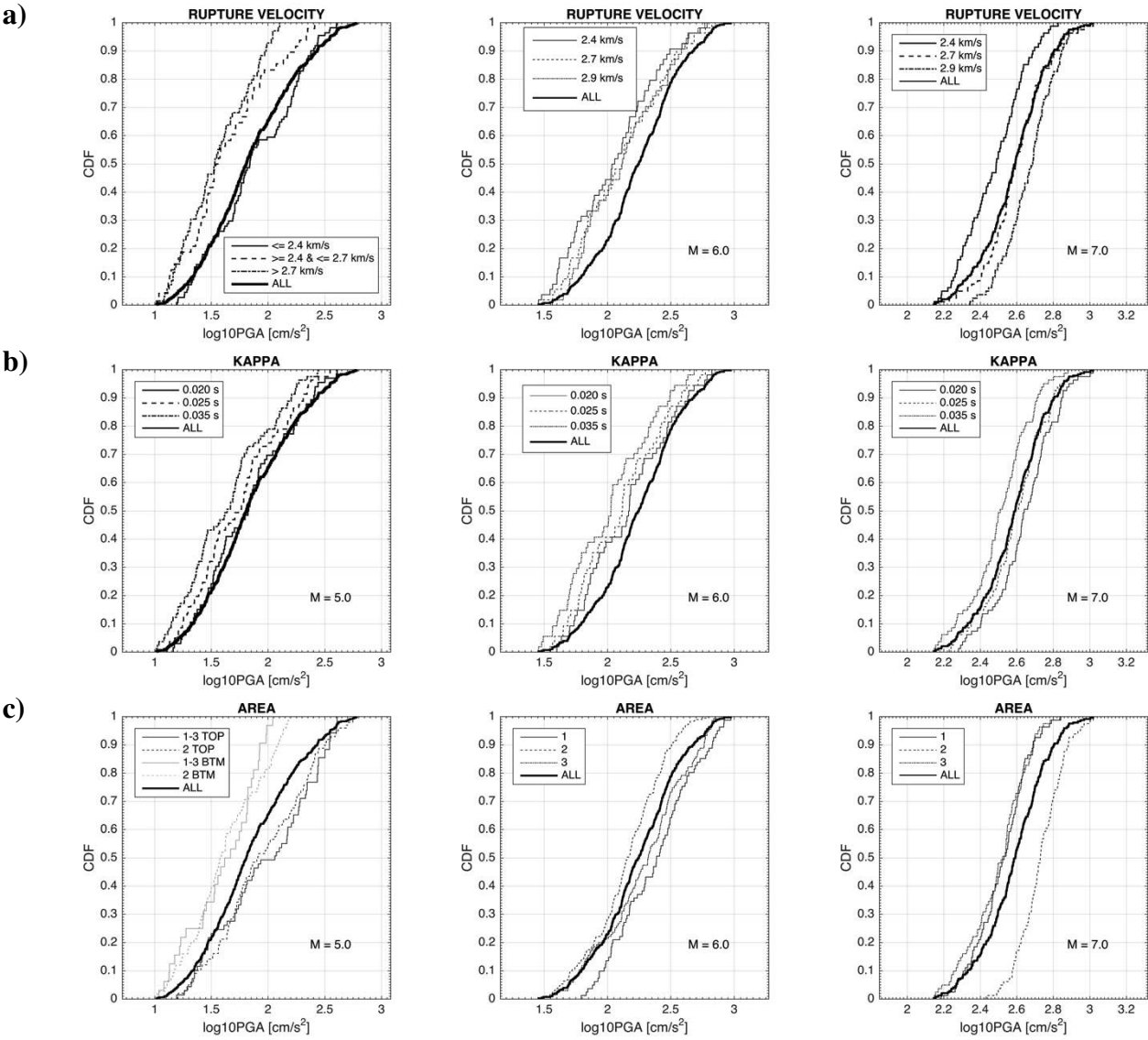


Figure 5

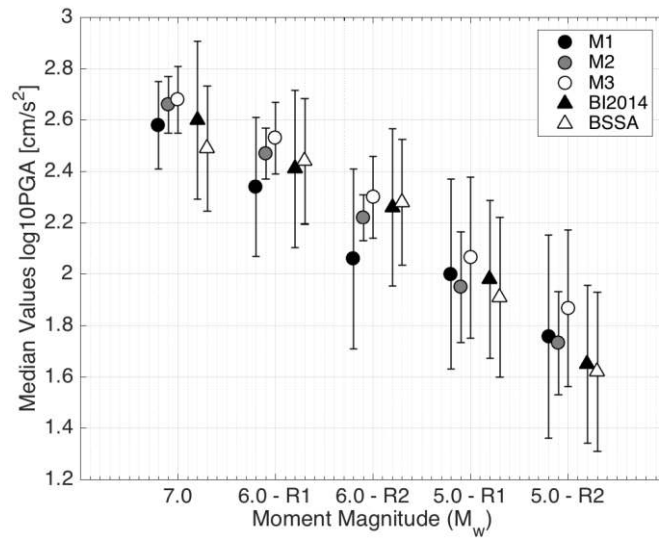


Figure 6a

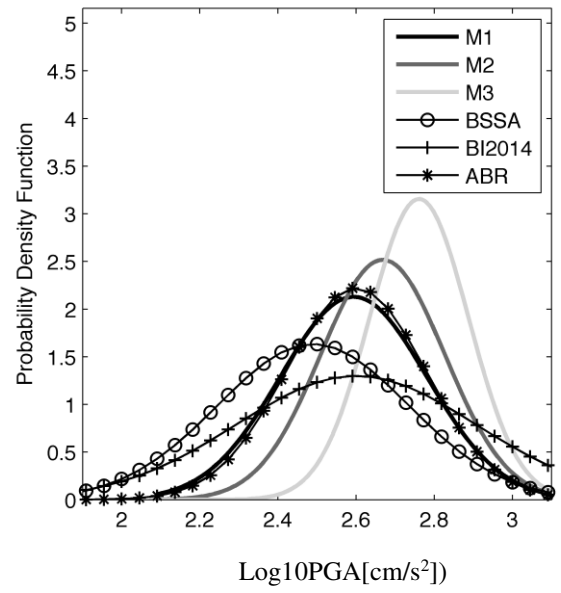
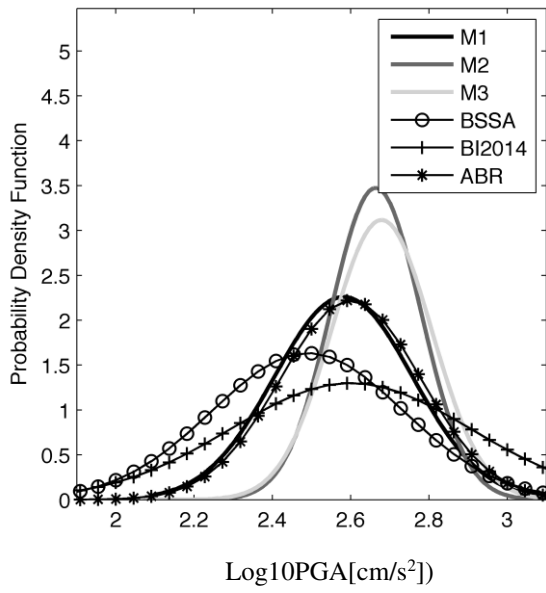


Figure 6b

Figure 6



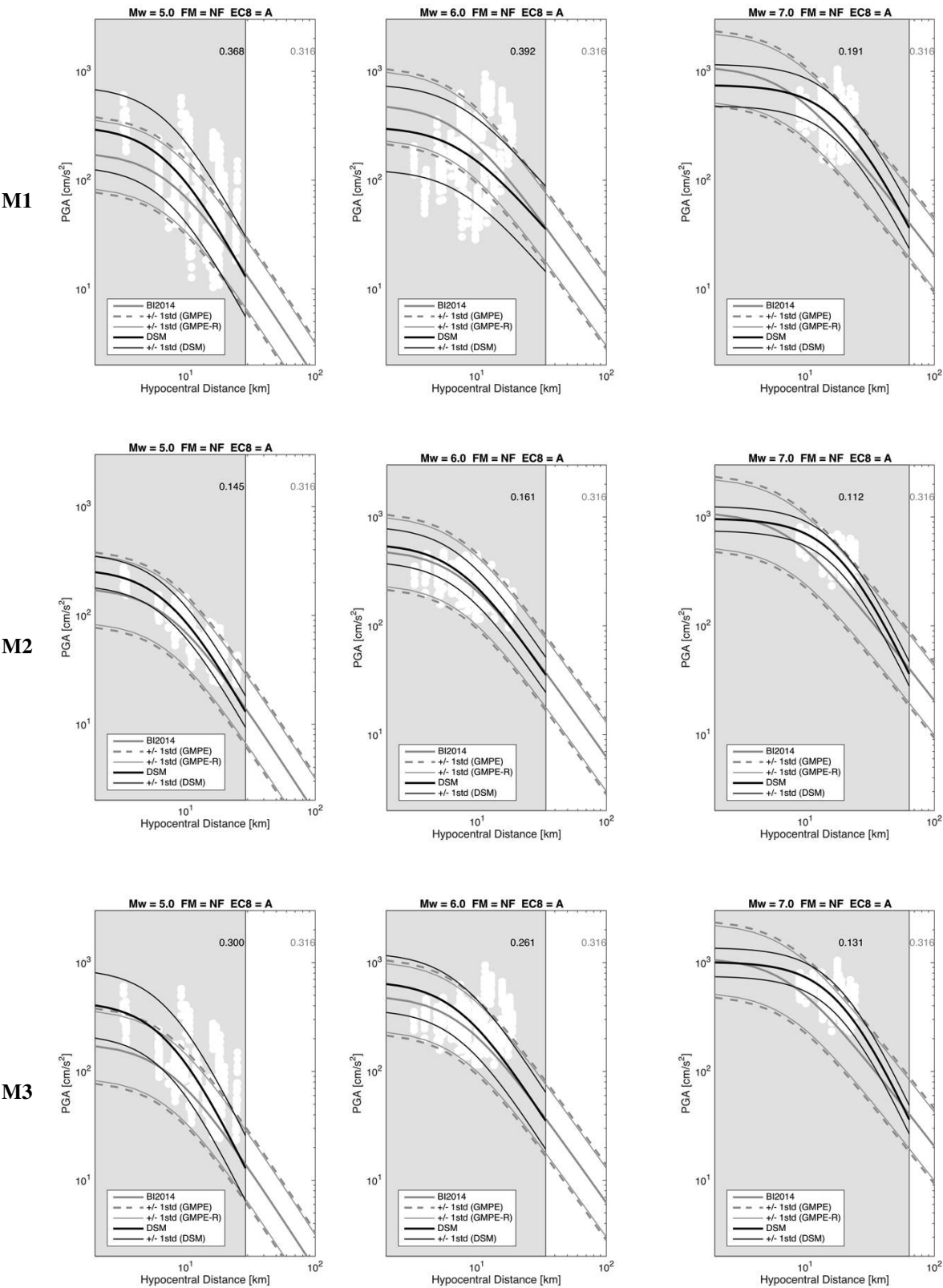
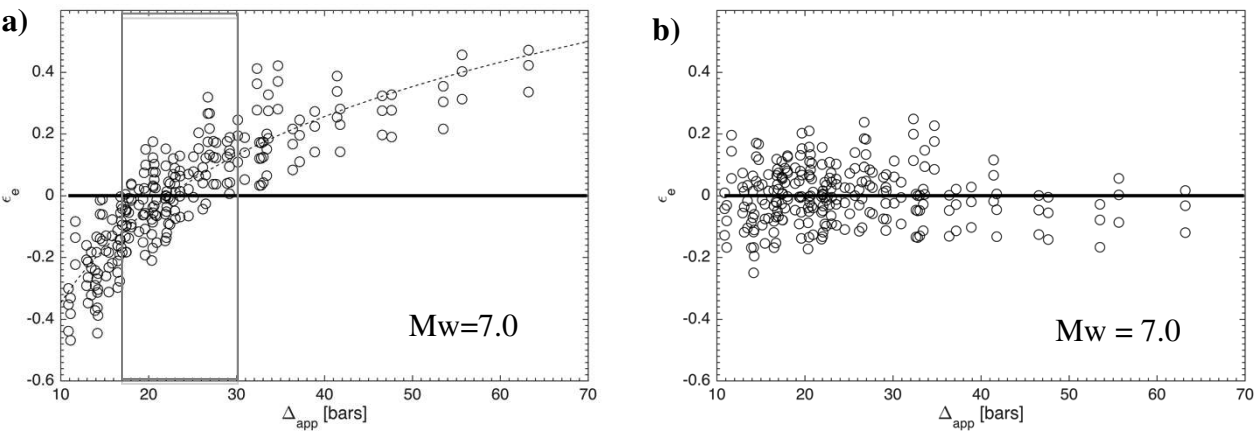


Figure 7

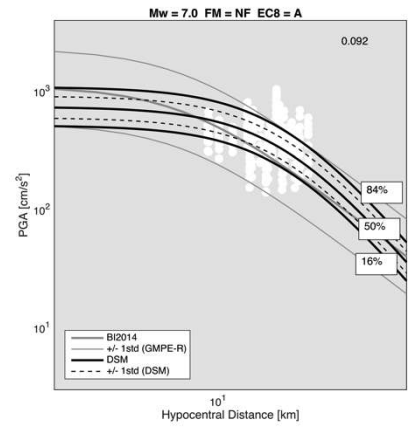
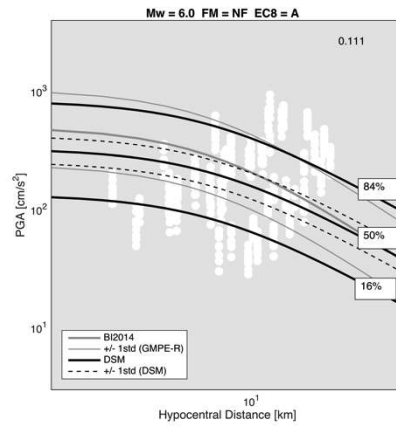
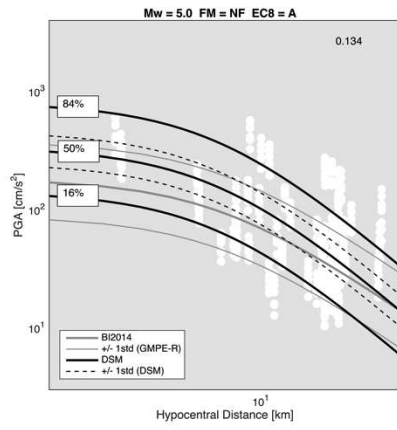
928



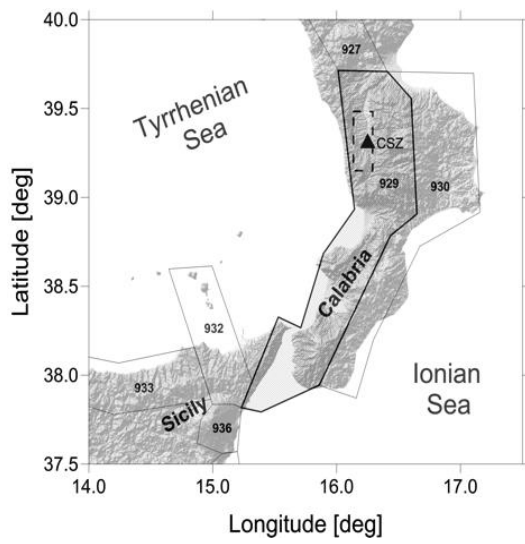
929

930

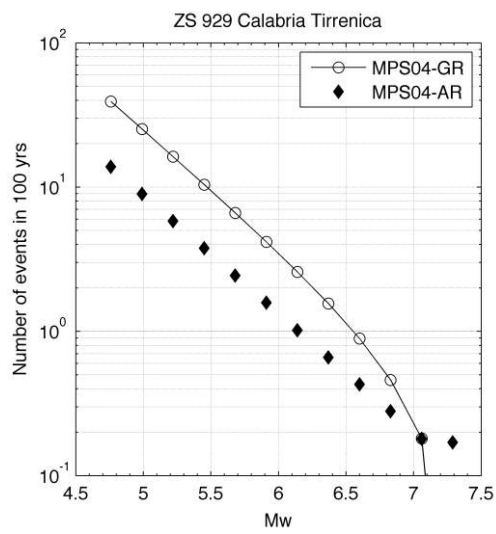
Figure 8



**Figure 9**



a)



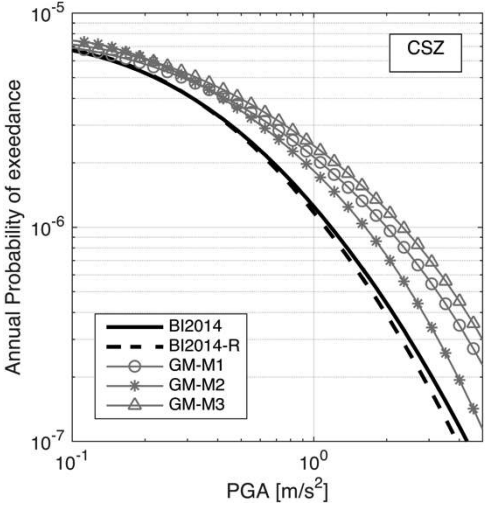
b)

Figure 10

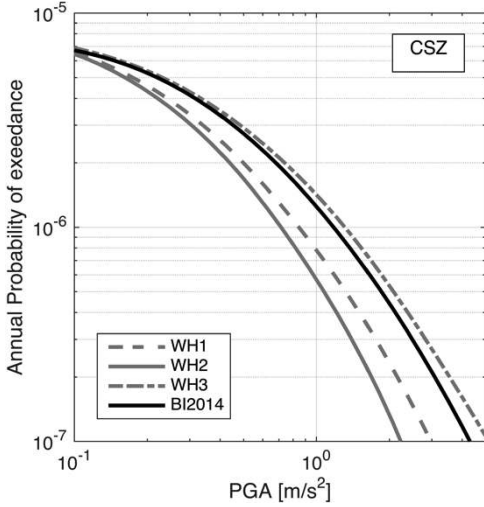
935

936

a)



b)



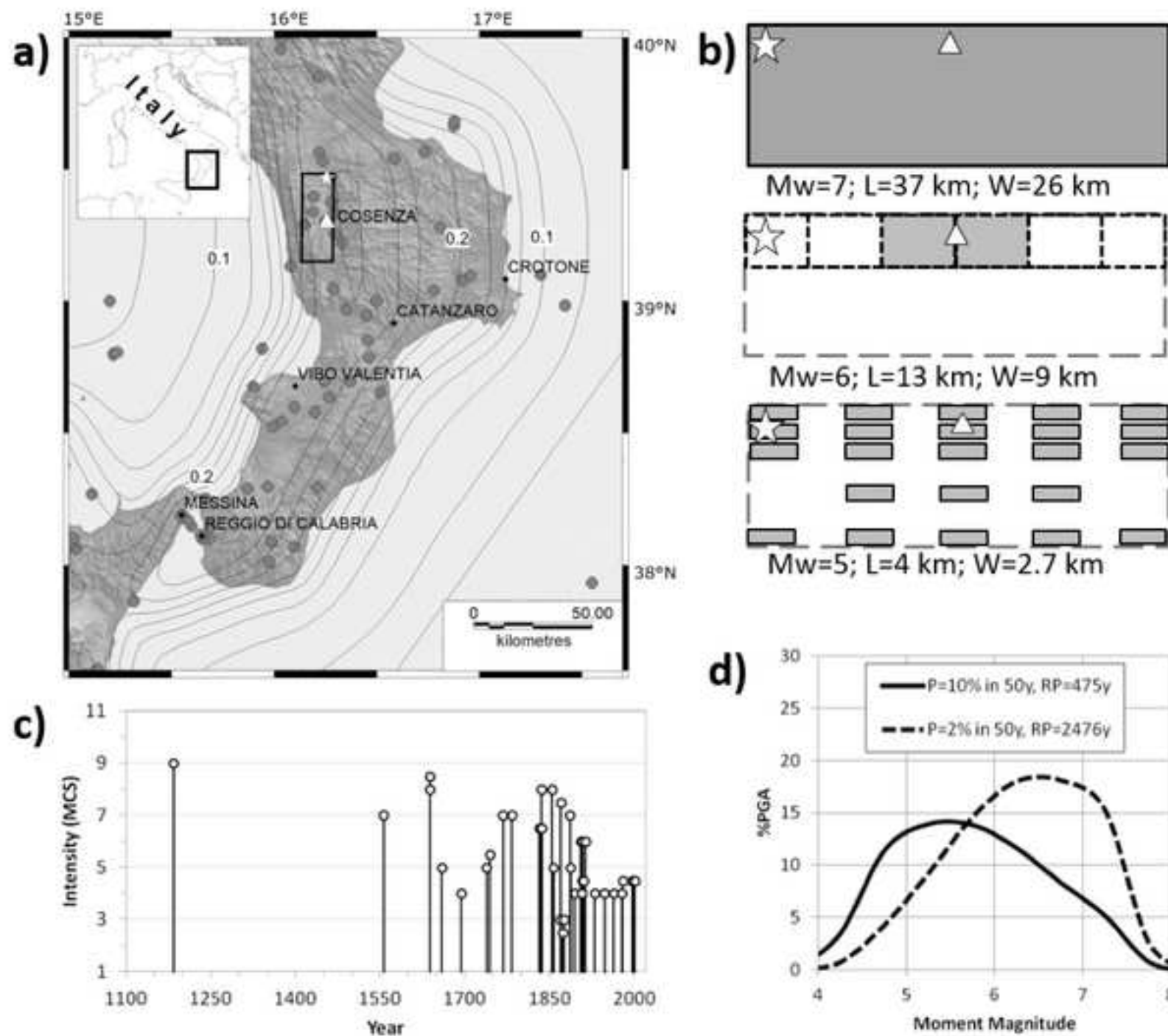
937

938

939

Figure 11

Figure 1

[Click here to download Figure Figure1.jpg](#)

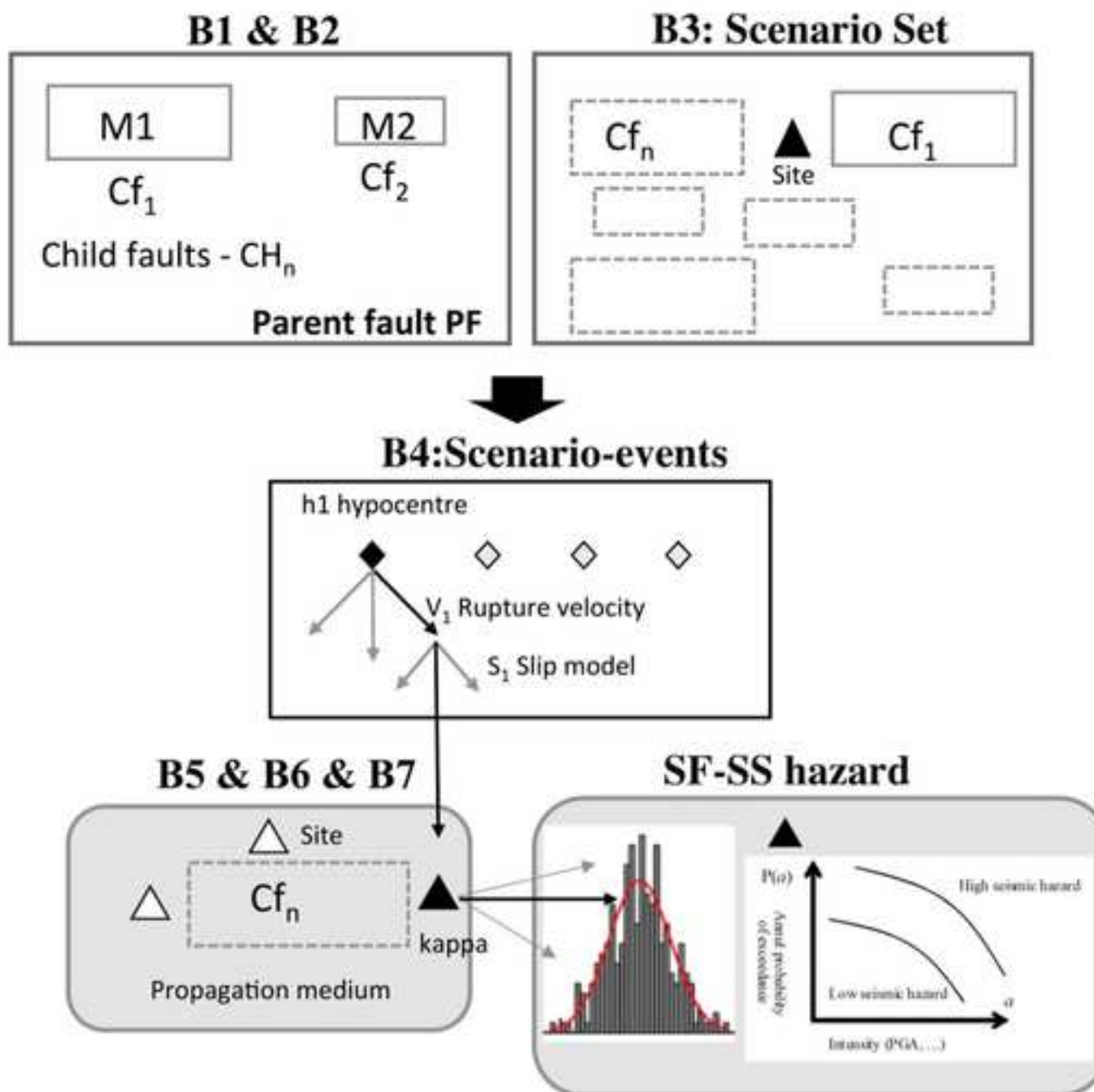


Figure 3

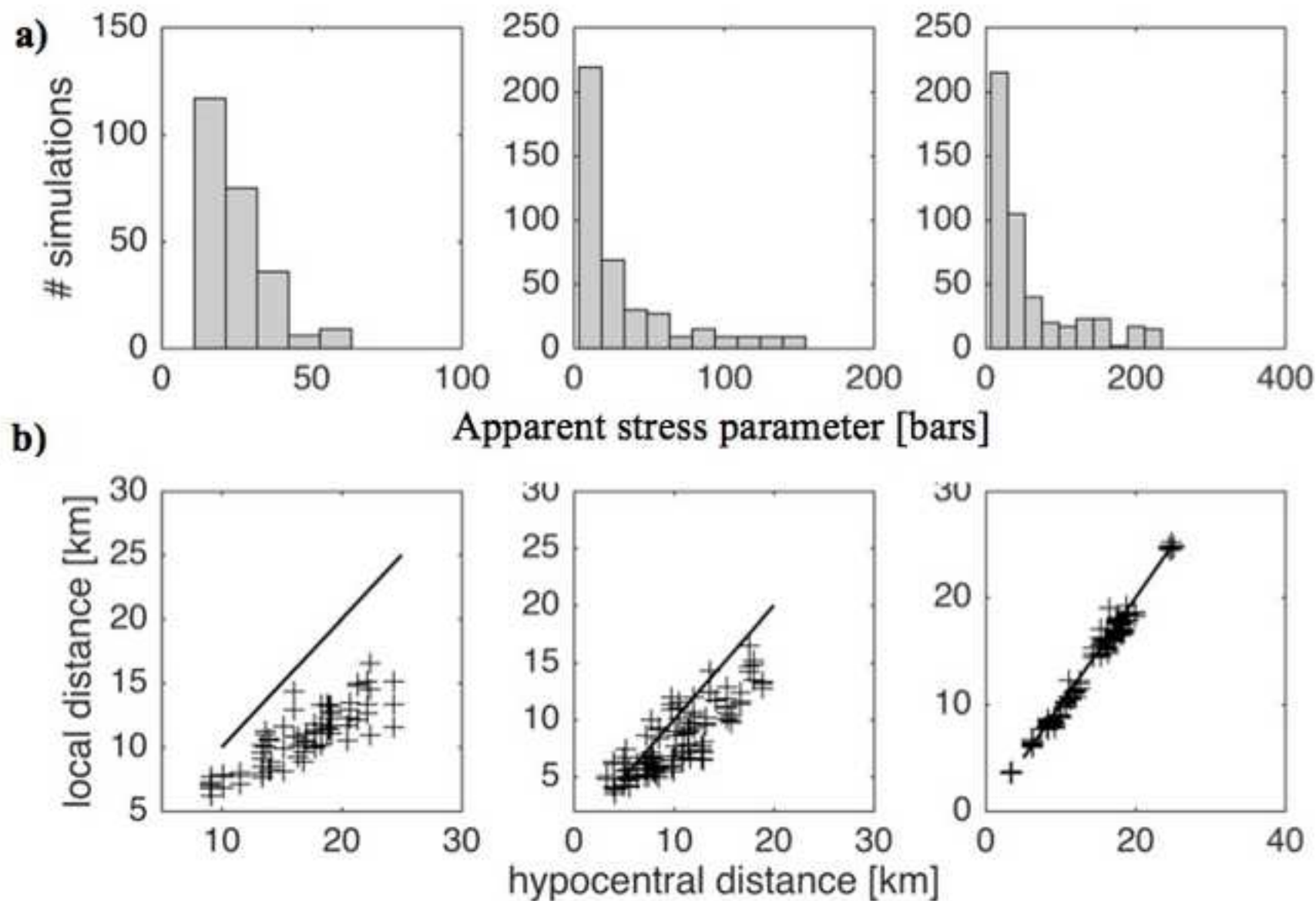




Figure 4

[Click here to download Figure4.jpg](#)

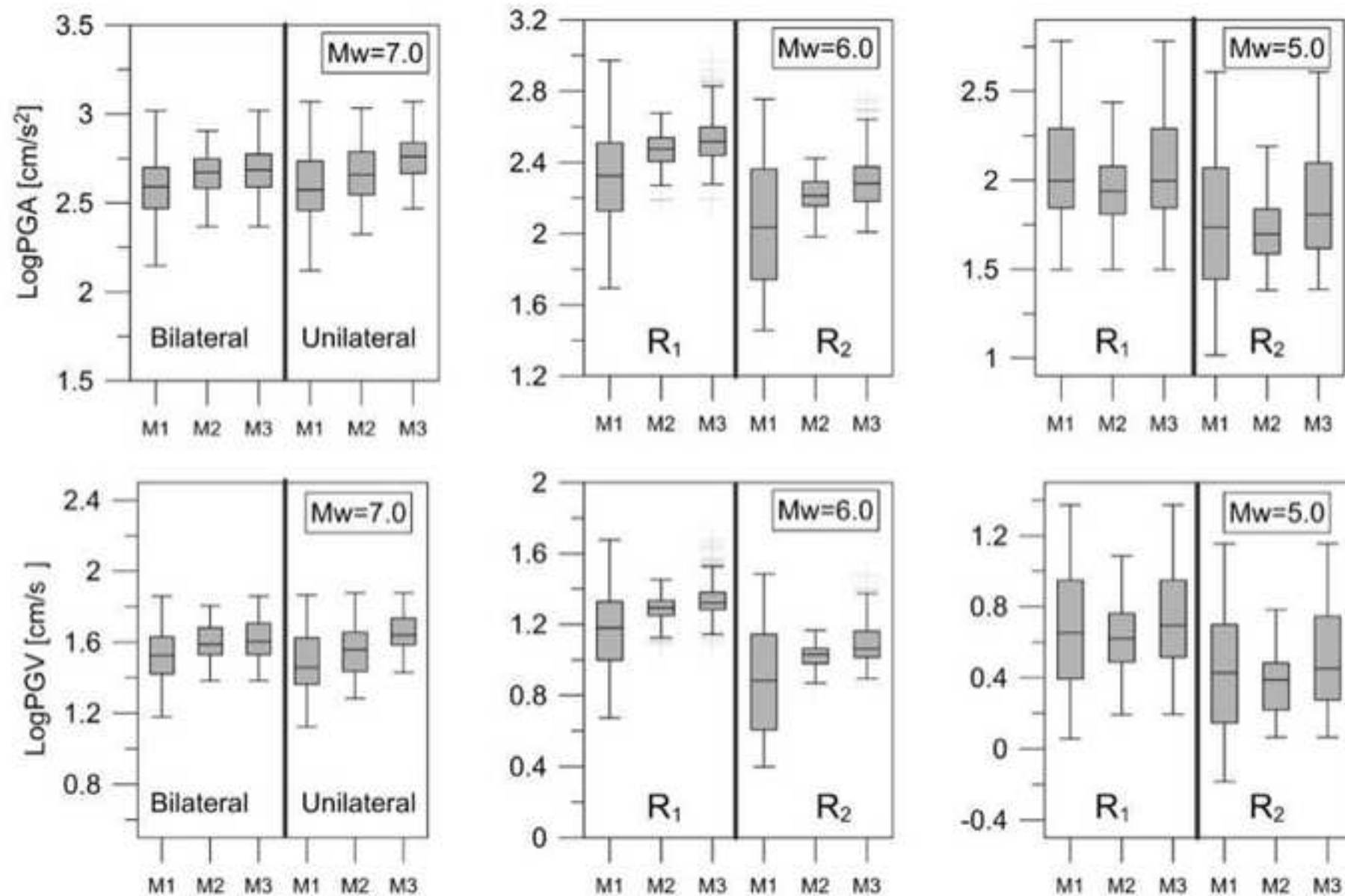


Figure 5

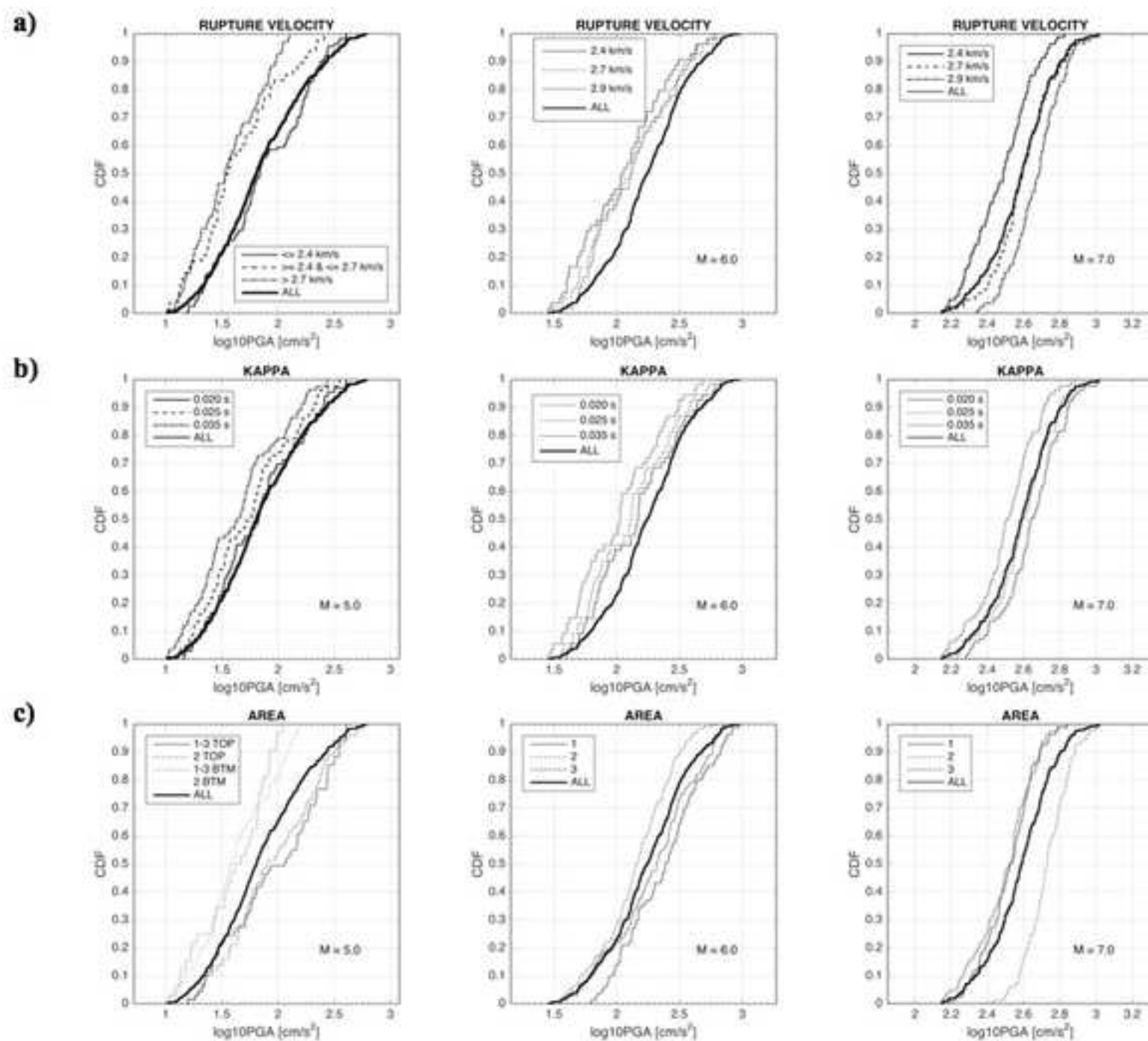
[Click here to download Figure5.jpg](#)

Figure 6a

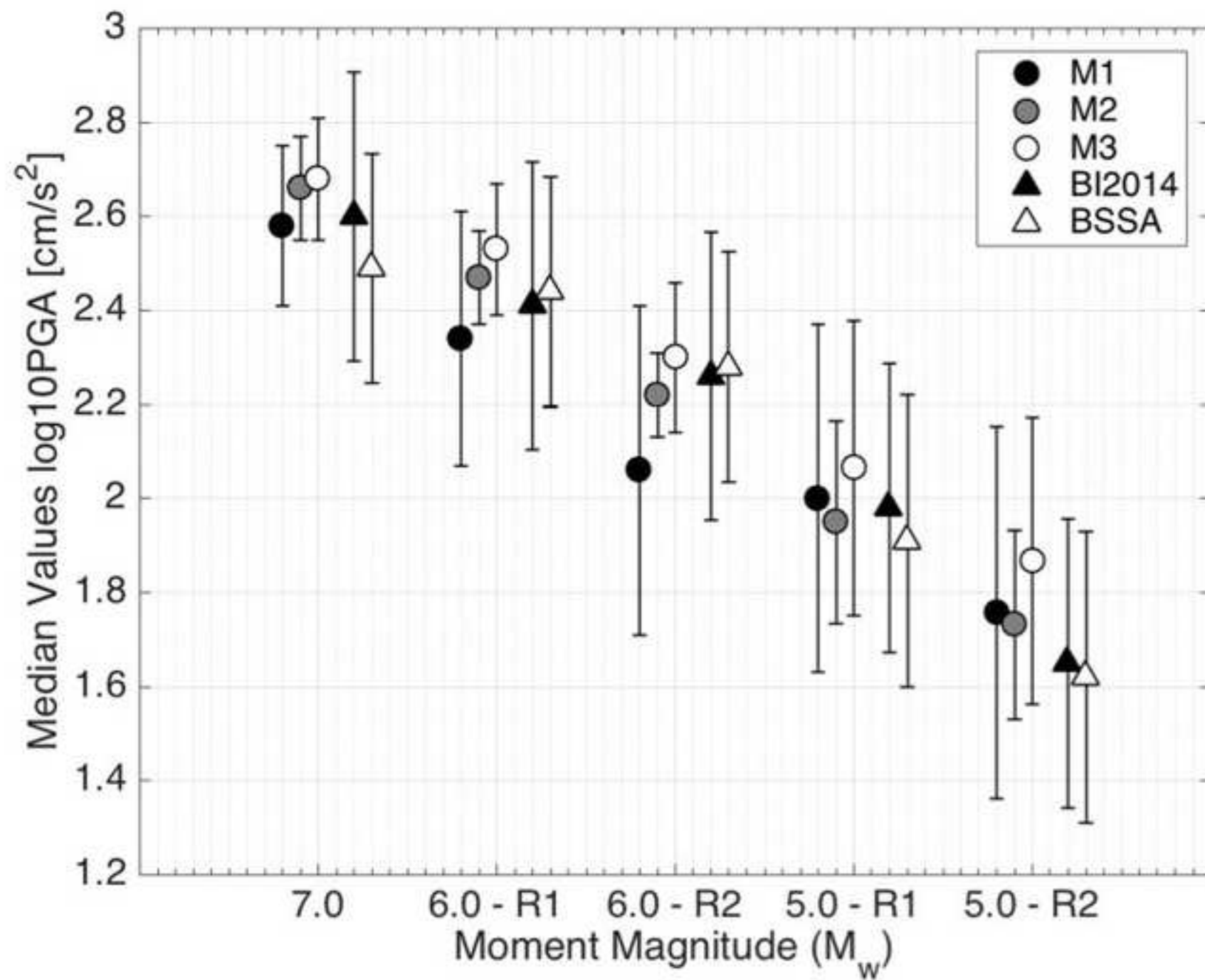
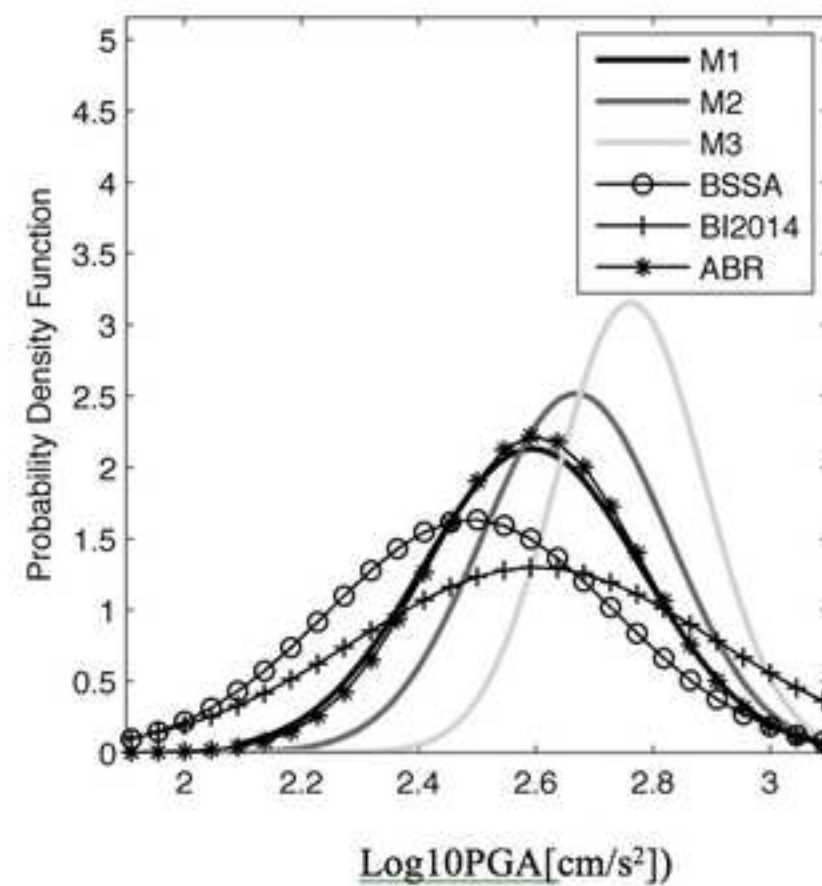
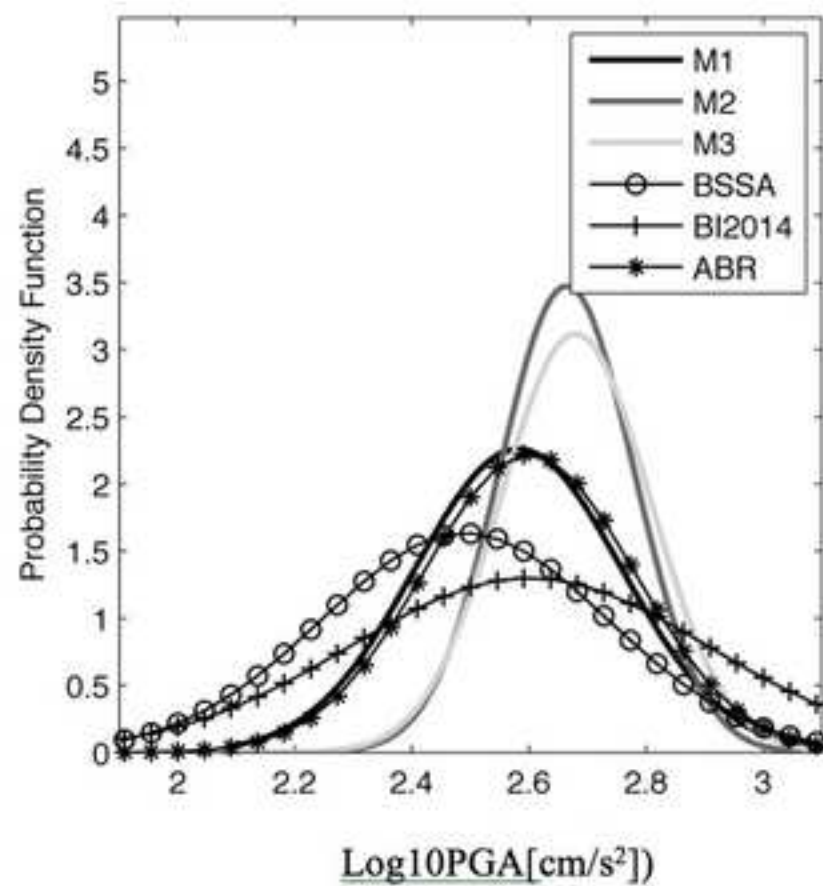
[Click here to download Figure Figure6a.jpg](#)

Figure 6b

[Click here to download Figure Figure6b.jpg](#)

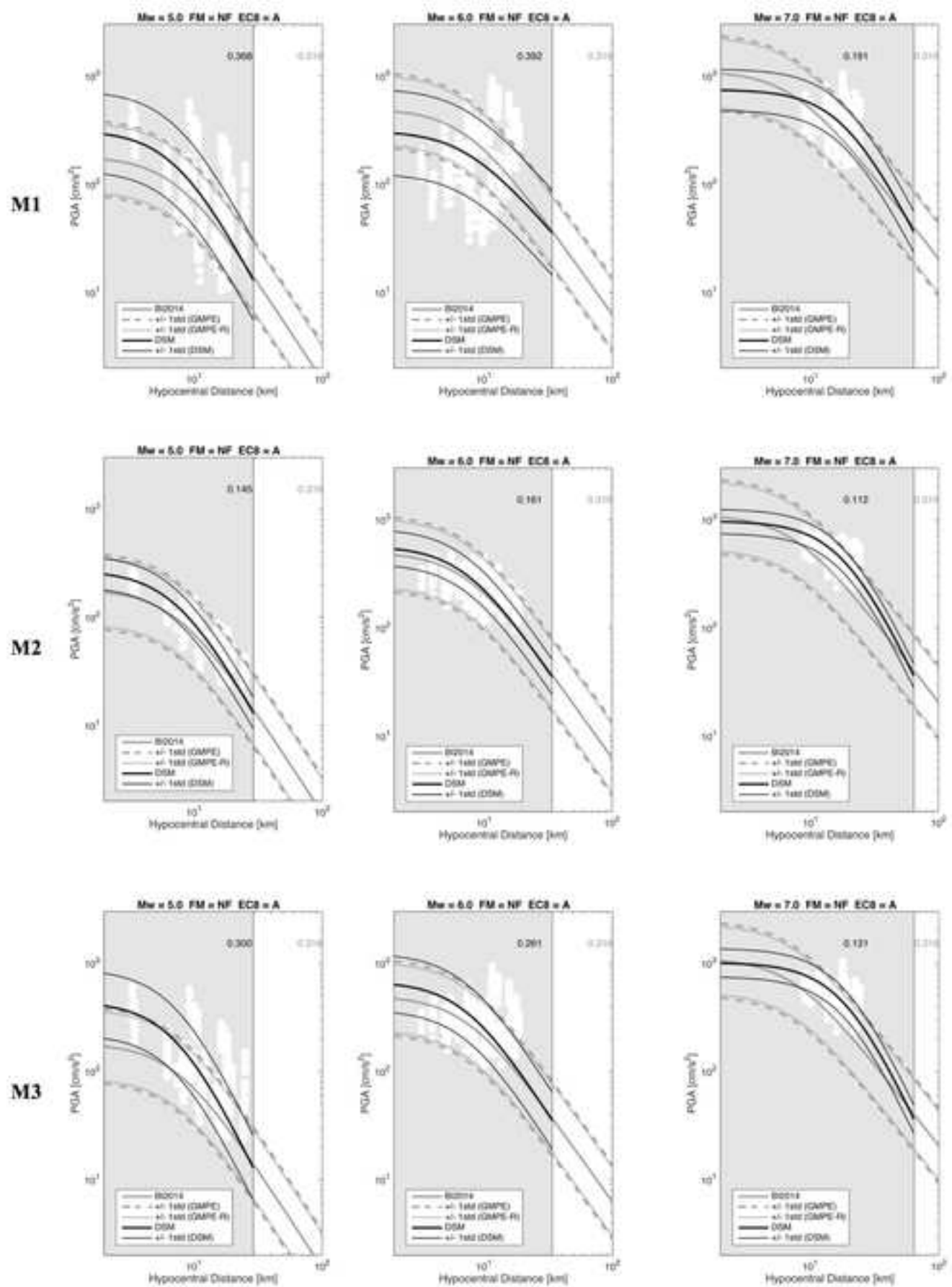
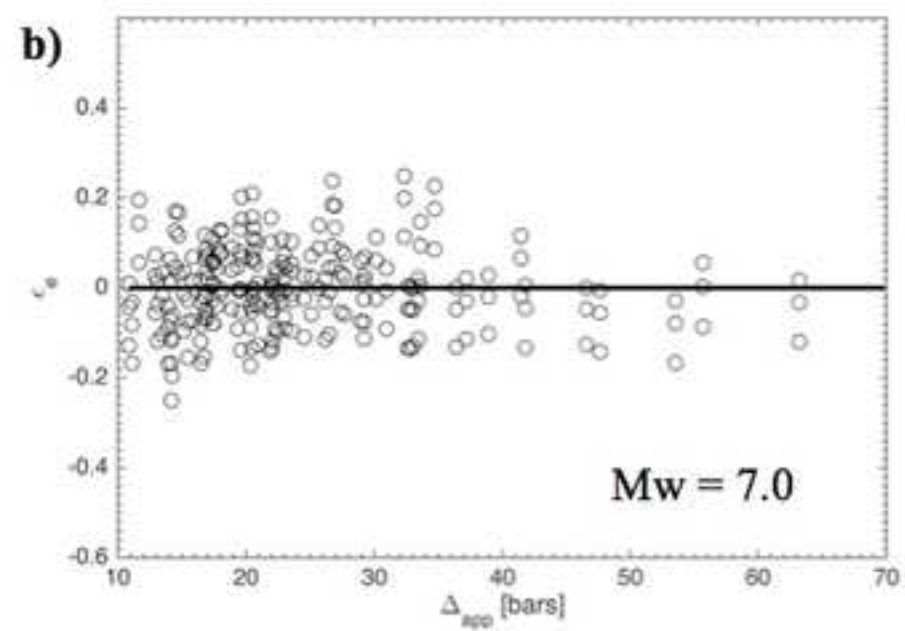
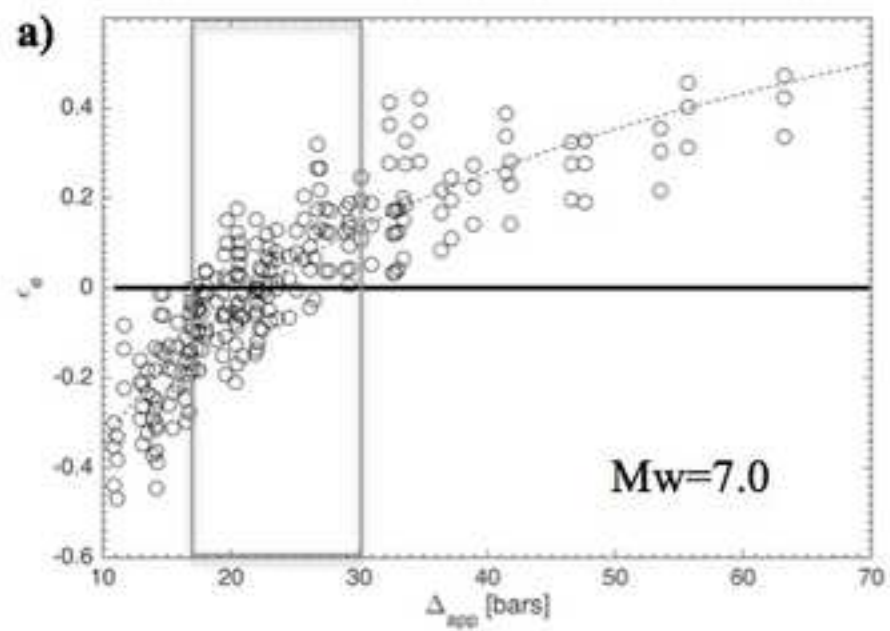
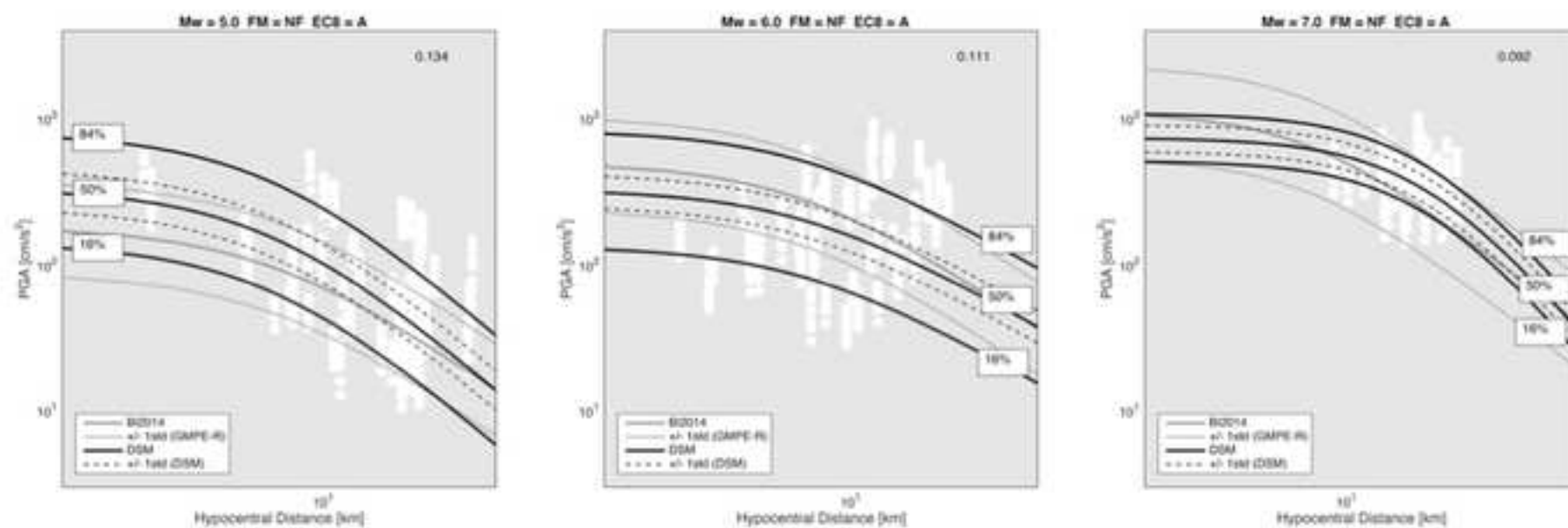
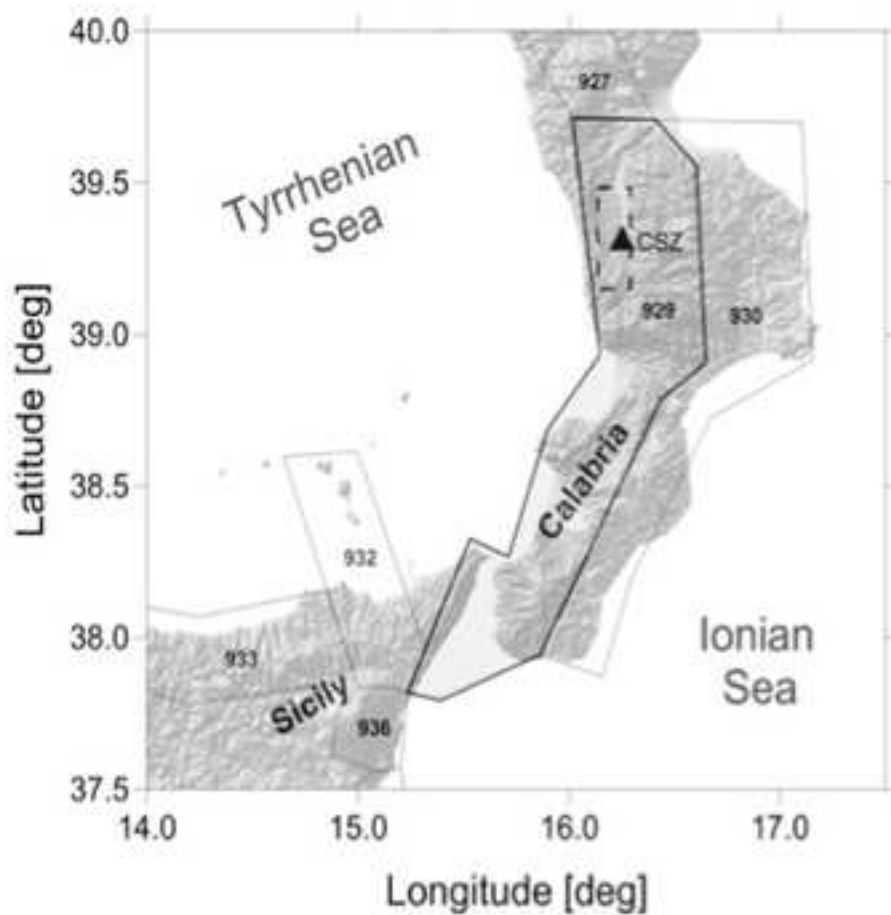
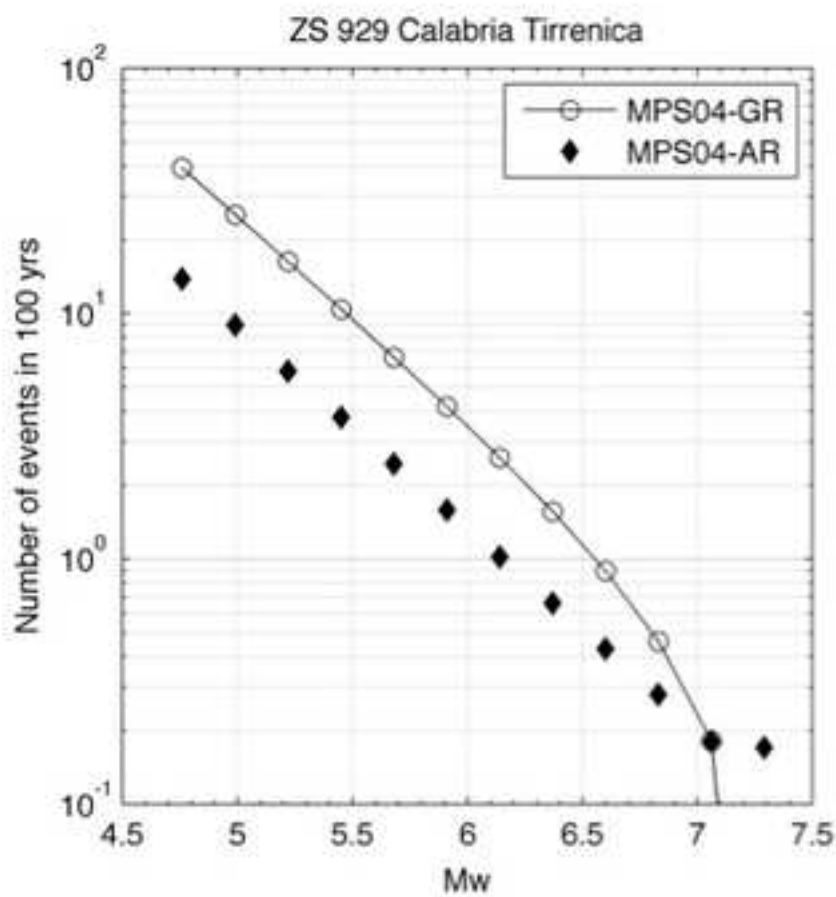


Figure 8

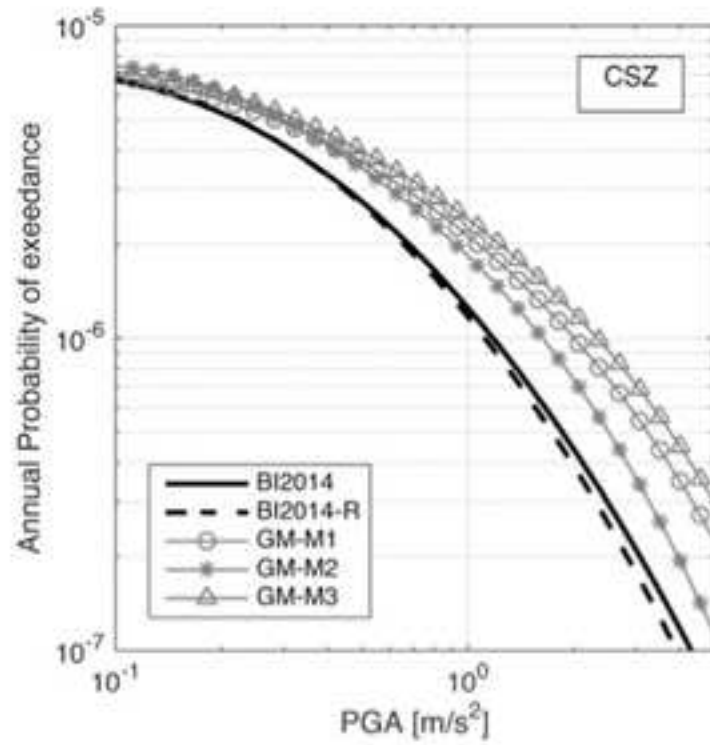
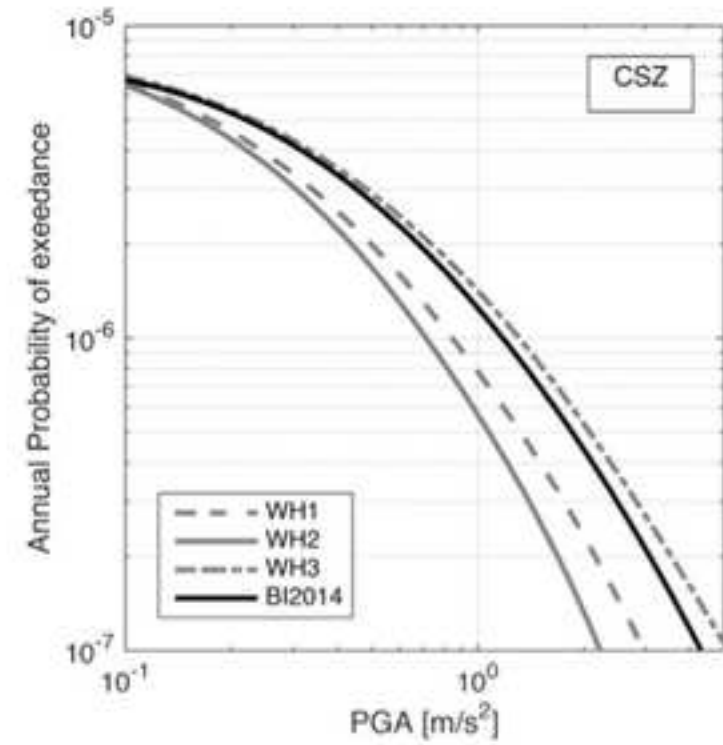






**a)****b)**



**a)****b)**

Electronic Supplement to

**Ground-Motion Variability for Single Site and Single Source through Deterministic Stochastic Method Simulations: implications for PSHA**

*Maria D'Amico, Mara Monica Tiberti, Emiliano Russo, Francesca Pacor, Roberto Basili*

We provide a detailed representation of the synthetic ground motion distributions for each magnitude and distance pairs considered in our analyses.

For M7.0 and M6.0, based on visual inspection and statistical tests (i.e. Kolmogorov test and  $\chi$ -square test with 5% confidence interval), the synthetic PGA follows, on average, a lognormal distribution, independently of the modeling setup (M1, M2, and M3). However, directivity effects can generate distributions characterized by either positive or negative skew (for example the PGA distributions at s001 relative to the M7.0 case). Compared to the PGAs, the PGV values are better described by multimodal distributions. For the M5.0 case we observe that, independently from the scenario model, the ground-motion parameter distributions can be only approximated by lognormal shapes both at high and at low frequencies; a larger number of CFs should be considered to better sample the PF to generate a lognormal distribution.

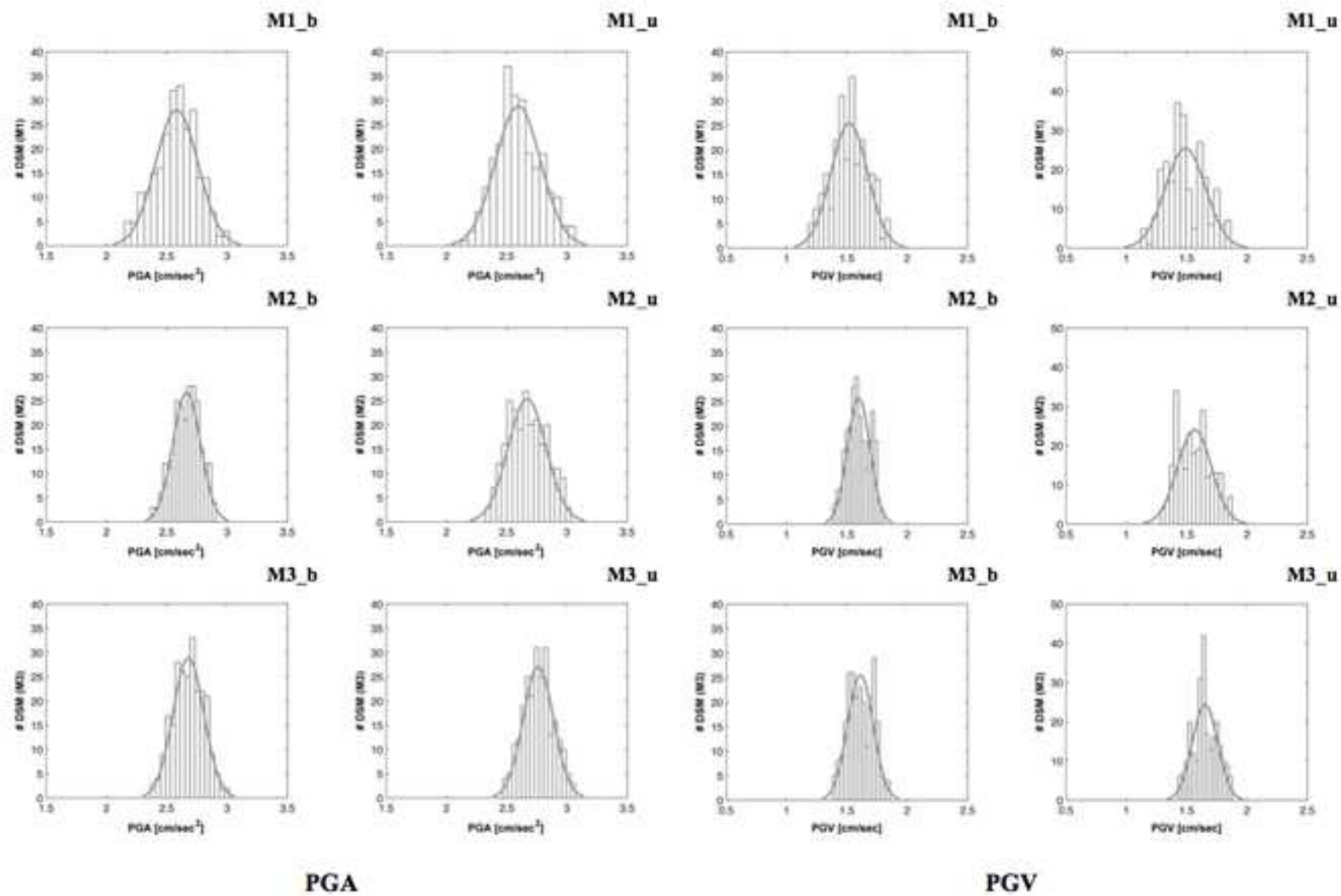
## Figure Captions

**Figure S1.** Histograms of the synthetic PGA and PGV (alternate columns) for M7.0 and  $R_{JB} = 0$  km, fitted by a normal distribution (grey line). Statistical distributions are for different scenario configurations: uppermost panels: finite-fault simulations with apparent corner frequency (M1); central panels: point-source simulations (M2); lowermost panels: merging between finite-fault and point-source simulations imposing a corner frequency threshold of 0.07 Hz (M3). Simulations were performed both at the bilateral site ( $_{b} = \text{CSZ}$ ) and at the quasi-unilateral site ( $_{u} = \text{s001}$ ).

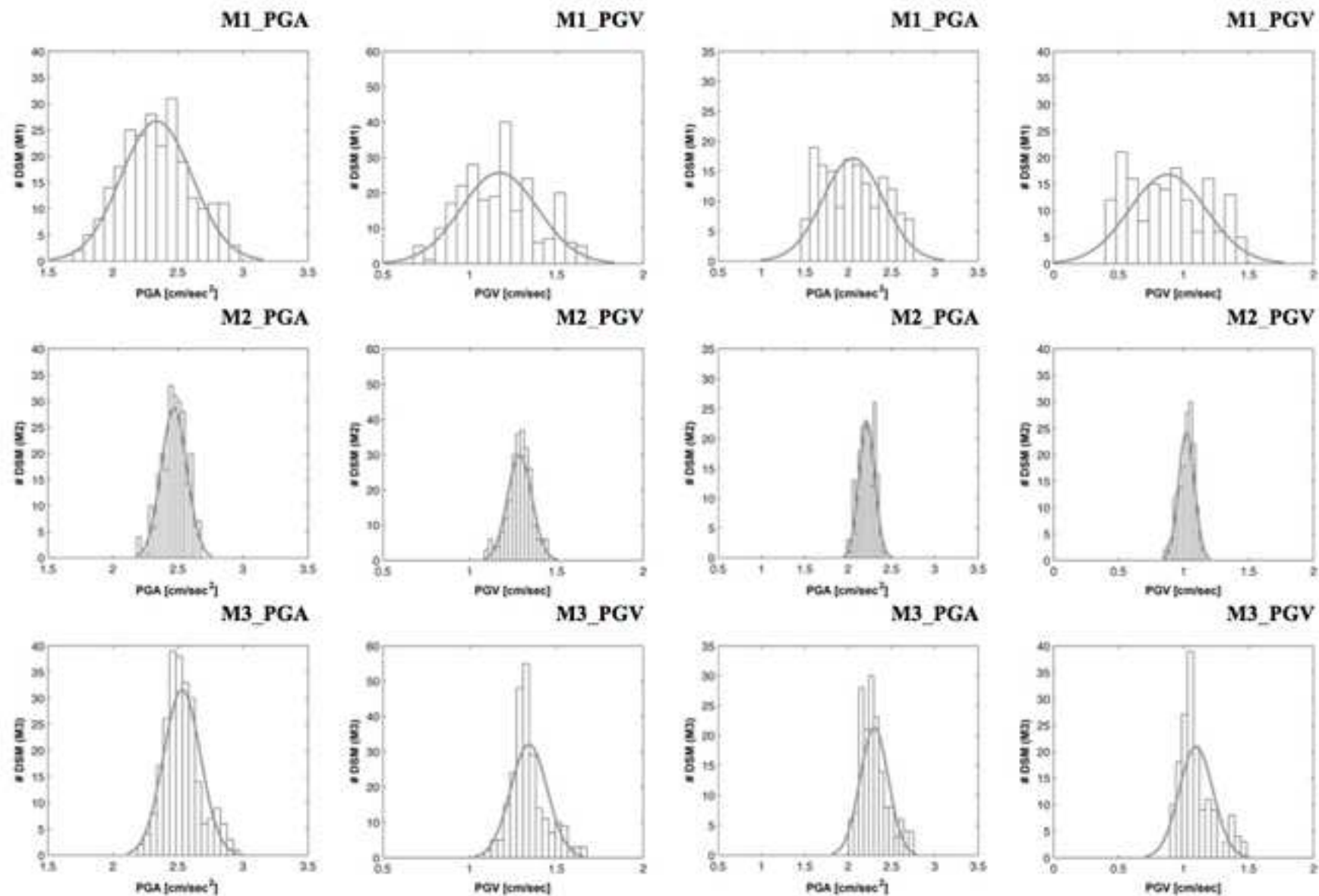
**Figure S2.** Histograms of the synthetic PGA and PGV (alternate columns) for M6.0 with respect to the CSZ site fitted by a normal distribution (grey line). Leftmost two columns:  $R_{JB} = 0$  km; Rightmost two columns: average  $R_{JB} = 5$  km. Statistical distributions are for different scenario configurations: uppermost panels: finite-fault simulations with apparent corner frequency (M1);

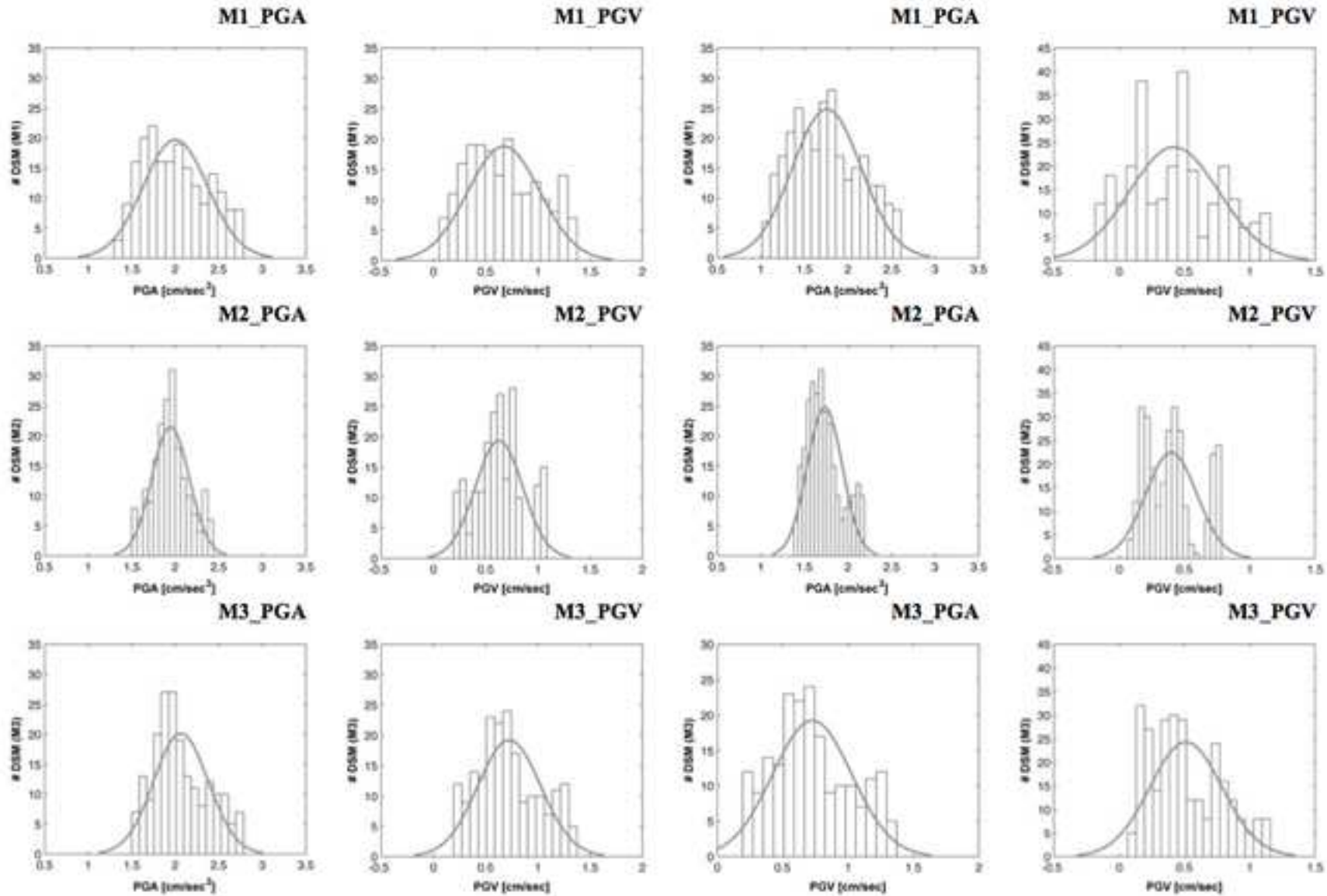
central panels: point-source simulations (M2); lowermost panels: merging between finite-fault and point-source simulations imposing a corner frequency threshold of 0.23 Hz (M3).

**Figure S3.** Histograms of the synthetic PGA and PGV (alternate columns) for M5.0 with respect to the CSZ site fitted by a normal distribution (grey line). Leftmost two columns: average  $R_{\text{epi}} = 5$  km; Rightmost two columns: average  $R_{\text{epi}} = 10$  km. Statistical distributions are for different scenario configurations: uppermost panels: finite-fault simulations with apparent corner frequency (M1); central panels: point-source simulations (M2); lowermost panels: merging between finite-fault and point-source simulations imposing a corner frequency threshold of 0.7 Hz (M3).

**M7.0**

6.0

 $R_{JB} = 0 \text{ km}$  $R_{JB} = 5 \text{ km}$

**M5.0** $R_{EPI} = 4 \text{ km}$  $R_{EPI} = 10 \text{ km}$

***Bulletin of the Seismological Society of America*****COPYRIGHT/PUBLICATION-CHARGES FORM**

PLEASE FILL OUT AND SUBMIT THIS FORM ONLINE WHEN SUBMITTING YOUR PAPER  
OR FAX IT TO FAX NUMBER 503 405 7190

Manuscript Number: BSSA-D- 15-00377R3 \_\_\_\_\_ [leave blank for new submissions]

Title: Ground-Motion Variability for Single Site and Single Source through Deterministic Stochastic Method Simulations: implications for PSHA

Authors: Maria D'Amico, Mara Monica Tiberti, Emiliano Russo, Francesca Pacor and Roberto Basili

**COPYRIGHT**

In accordance with Public Law 94-533, copyright to the article listed above is hereby transferred to the Seismological Society of America (for U.S. Government employees, to the extent transferable) effective if and when the article is accepted for publication in the *Bulletin of the Seismological Society of America*. The authors reserve the right to use all or part of the article in future works of their own. In addition, the authors affirm that the article has not been copyrighted and that it is not being submitted for publication elsewhere.

To be signed by at least one of the authors (who agrees to inform the others, if any) or, in the case of "work made for hire," by the employer.



Authorized Signature for Copyright

Print Name (and title, if not author)

29/11/2016

Date

**PUBLICATION CHARGES**

The Seismological Society of America requests that institutions supporting research share in the cost of publicizing the results of that research. The Editor has the discretion of waiving publication charges for authors who do not have institutional support. In addition to regular publication charges there is a nominal fee for publishing electronic supplements. Current rates are available at <http://www.seismosoc.org/publications/bssa/authors/bssa-page-charges.php>

**Color options:** Color figures can be published (1) in color both in the online journal and in the printed journal, or (2) in color online and gray scale in print. Online color is free; authors will be charged for color in print. You must choose one option for all of the color figures within a paper; that is, you cannot choose option (1) for one color figure and option (2) for another color figure. You cannot submit two versions of the same figure, one for color and one for gray scale. You are responsible for ensuring that color figures are understandable when converted to gray scale, and that text references and captions are appropriate for both online and print versions. Color figures must be submitted before the paper is accepted for publication.

Art guidelines are at <http://www.seismosoc.org/publications/bssa/authors/bssa-art-submissions.php>

Will publication charges be paid? Check one:

☐ **BOTH PUBLICATION CHARGES AND COLOR CHARGES WILL BE PAID**, and all color figures for this paper will be color both online and in print. This option requires full payment of publication & color charges.

☒ **ONLY PUBLICATION CHARGES WILL BE PAID**, and all figures for this paper will be gray scale in print. Color figures, if any, will be color online.

☐ **REQUEST A REDUCTION IN PUBLICATION CHARGES.** Send a letter of request and explanation to the Editor-in-Chief at [BSSA@seismosoc.org](mailto:BSSA@seismosoc.org). Color figures, if any, will be color online but grey scale in print.

Send Invoice to: Istituto Nazionale di Geofisica e Vulcanologia, Via Corti 12, 20133, Milano, Italy

If your paper is accepted for publication, SSA requires that you fill out and submit an online billing/offprint form.

Questions regarding billing should be directed to the SSA Business Office,  
400 Evelyn Avenue, Suite 201 Albany, CA 94706 USA Phone 510 525-5474 Fax 510 525-7204